


Sulfide oxidation promotes hypoxic angiogenesis and neovascularization

Received: 13 March 2023

Accepted: 20 February 2024

Published online: 20 March 2024

 Check for updates

Roshan Kumar¹, Victor Vitvitsky¹, Apichaya Sethaudom¹, Rashi Singhal², Sumeet Solanki², Sydney Alibeckoff¹, Harrison L. Hiraki³, Hannah N. Bell², Anthony Andren², Brendon M. Baker^{3,4}, Costas A. Lyssiotis^{2,5,6}, Yatrik M. Shah^{1,2,5,6} & Ruma Banerjee¹✉

Angiogenic programming in the vascular endothelium is a tightly regulated process for maintaining tissue homeostasis and is activated in tissue injury and the tumor microenvironment. The metabolic basis of how gas signaling molecules regulate angiogenesis is elusive. Here, we report that hypoxic upregulation of $\cdot\text{NO}$ in endothelial cells reprograms the transsulfuration pathway to increase biogenesis of hydrogen sulfide (H_2S), a proangiogenic metabolite. However, decreased H_2S oxidation due to sulfide quinone oxidoreductase (SQOR) deficiency synergizes with hypoxia, inducing a reductive shift and limiting endothelial proliferation that is attenuated by dissipation of the mitochondrial NADH pool. Tumor xenografts in whole-body ($\text{WB}^{\text{Cre}}\text{Sqor}^{\text{fl/fl}}$) and endothelial-specific (VE-cadherin^{Cre-ERT2} $\text{Sqor}^{\text{fl/fl}}$) Sqor -knockout mice exhibit lower mass and angiogenesis than control mice. $\text{WB}^{\text{Cre}}\text{Sqor}^{\text{fl/fl}}$ mice also exhibit decreased muscle angiogenesis following femoral artery ligation compared to control mice. Collectively, our data reveal the molecular intersections between H_2S , O_2 and $\cdot\text{NO}$ metabolism and identify SQOR inhibition as a metabolic vulnerability for endothelial cell proliferation and neovascularization.

Angiogenesis is a complex process that is essential for embryonic development and wound repair in adults¹. Dysregulation of this process is associated with the pathogenesis of infectious, malignant, ischemic, inflammatory and immune diseases^{2,3}. Despite the anticipated promise of early antiangiogenic therapeutics for treating disorders ranging from cancer to blindness⁴, these drugs have shown limited efficacy, highlighting the need for alternative, and preferably combination, therapies to counteract issues with resistance and/or neovascularization via other pathways⁵. Hydrogen sulfide (H_2S) is a proangiogenic metabolite^{6,7} that interacts with the nitric oxide ($\cdot\text{NO}$)-dependent cGMP signaling pathway⁸ and increases endothelial cell growth and migration via phosphorylation of ERK, AKT and p38 (ref. 9). Vascular endothelial growth factor (VEGF) reportedly stimulates H_2S release⁹. However,

sulfur amino acid restriction also serves as a proangiogenic trigger, paradoxically increasing H_2S synthesis in addition to VEGF expression, signaling via the GCN2–ATF4 amino acid starvation pathway¹⁰. Although $\cdot\text{NO}$ - and carbon monoxide-dependent hypoxic increases in H_2S synthesis have been reported^{11,12}, the mechanism of $\cdot\text{NO}$ -dependent regulation of H_2S synthesis in endothelial cells and the potential role of sulfide oxidation in angiogenesis are poorly understood.

H_2S is a product of the transsulfuration pathway enzymes cystathionine β -synthase (CBS) and γ -cystathionase (γ -CTH¹³; Fig. 1a). The transsulfuration pathway plays a key role in regulating levels of the thrombogenic amino acid homocysteine as well as in furnishing cysteine, the limiting substrate for glutathione (GSH) synthesis^{14,15}. The pathway is also a source of H_2S , which inhibits complex IV and

¹Department of Biological Chemistry, University of Michigan, Ann Arbor, MI, USA. ²Department of Molecular and Integrative Physiology, University of Michigan, Ann Arbor, MI, USA. ³Department of Biomedical Engineering, University of Michigan, Ann Arbor, MI, USA. ⁴Department of Chemical Engineering, University of Michigan, Ann Arbor, MI, USA. ⁵Department of Internal Medicine, University of Michigan, Ann Arbor, MI, USA. ⁶Rogel Cancer Center, University of Michigan, Ann Arbor, MI, USA. ✉e-mail: rbanerje@umich.edu

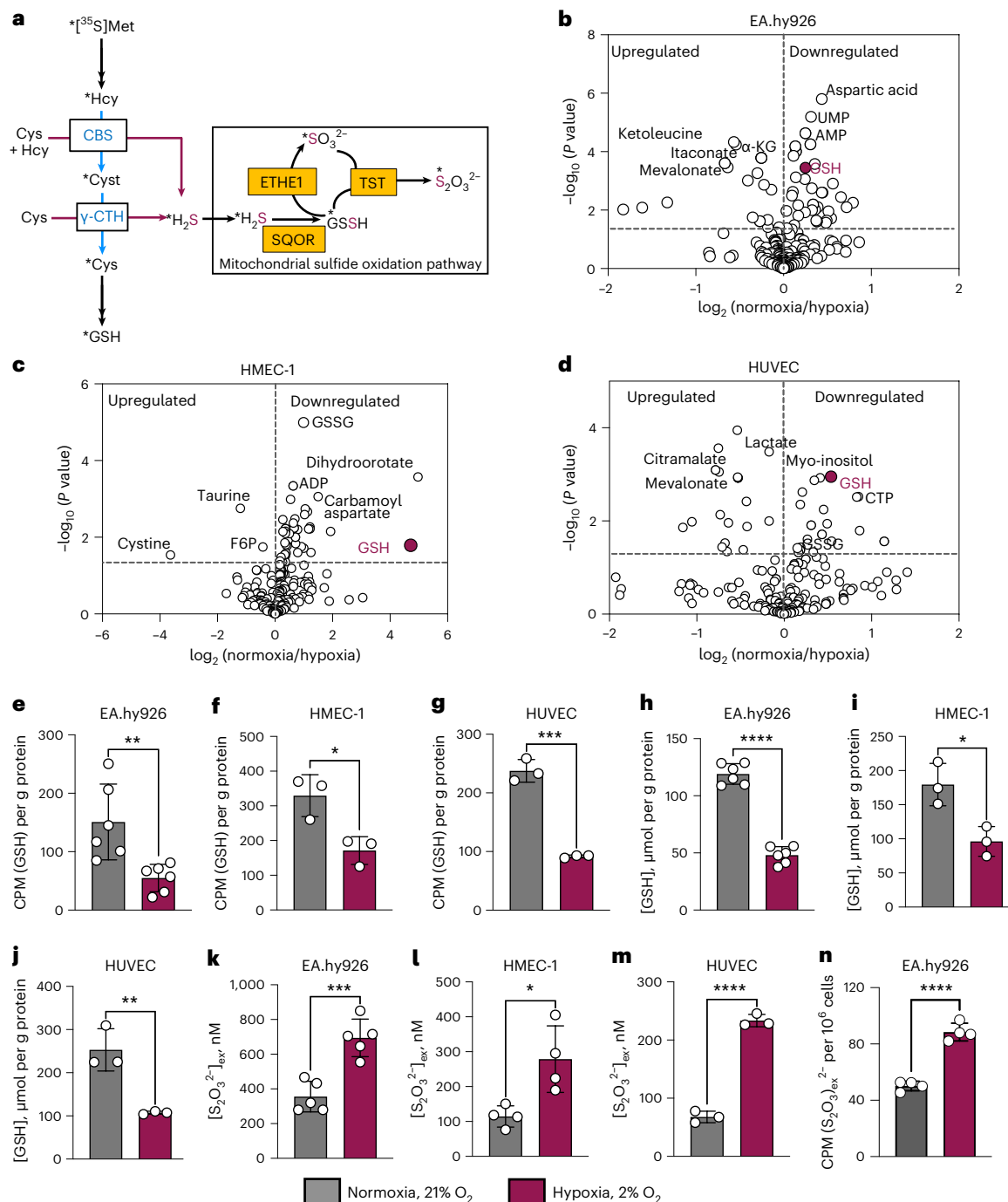


Fig. 1 | Hypoxic track switching in the transsulfuration pathway. **a**, Scheme showing radiolabel transfer from $[^{35}\text{S}]\text{methionine}$ ($[^{35}\text{S}]\text{Met}$) to GSH (asterisks) via the canonical transsulfuration pathway (blue arrows), H_2S synthesis (red arrows) and mitochondrial oxidation reactions; Cys, cystathionine; Hcy, homocysteine; TST, thiosulfate sulfurtransferase. **b-d**, Volcano plots reveal that GSH is significantly decreased in EA.hy926 cells (**b**), HMEC-1 cells (**c**) and HUVECs (**d**) grown under hypoxic versus normoxic conditions ($n = 4$ biologically independent samples). The horizontal lines in **b-d** represent a P value of 0.05, which was derived from a two-sample t -test with unequal variance; each metabolite is represented as the ratio of mean values on a \log_2 scale; α -KG, α -ketoglutarate; F6P, fructose-6-phosphate. **e-g**, $[^{35}\text{S}]\text{Methionine}$ incorporation

into GSH is lower under hypoxia than under normoxia in the indicated cell lines ($n = 6$ (**e**), $n = 3$ (**f**) and $n = 3$ (**g**)); $*P = 0.02$, $**P = 0.007$ and $***P = 0.0002$.

h-j, GSH concentration ($[\text{GSH}]$) is lower in the indicated cell lines ($n = 6$ (**h**), $n = 3$ (**i**) and $n = 3$ (**j**)); $*P = 0.02$, $**P = 0.007$ and $****P < 0.0001$. **k-m**, Extracellular thiosulfate ($[\text{S}_2\text{O}_3^{2-}]_{\text{ex}}$) levels are higher in the indicated cell lines under hypoxia than under normoxia ($n = 5$ (**k**), $n = 4$ (**l**) and $n = 3$ (**m**)); $*P = 0.017$, $***P = 0.0006$ and $****P < 0.0001$. **n**, $[^{35}\text{S}]\text{Methionine}$ flux into thiosulfate ($n = 4$); $****P < 0.0001$. Samples in **e-n** were collected either at 24 h (EA.hy926 and HMEC-1 cells) or at 16 h (HUVECs). Data represent mean values \pm s.d. in **e-n**. Statistics were derived from unpaired two-sided Student's t -tests; CPM, counts per minute. n denotes the number of independent experiments.

modulates cellular energetics^{16,17}. In their canonical roles, CBS and γ -CTH catalyze sulfur transfer from homocysteine to serine, forming cystathionine, which is subsequently metabolized to cysteine, α -ketobutyrate and ammonia. Additionally, CBS and γ -CTH exhibit

substrate promiscuity, leading to noncanonical reactions that generate H_2S from cysteine and/or homocysteine¹⁸. Individuals with CBS deficiency exhibit elevated plasma homolanthionine¹⁹ as a result of the γ -CTH-catalyzed condensation of two moles of homocysteine²⁰.

The regulatory heme cofactor in human CBS sensitizes it to inhibition by carbon monoxide or $\cdot\text{NO}$, decreasing cystathionine synthesis^{21,22}, which in turn promotes H_2S synthesis by γ -CTH-mediated catabolism of cysteine²³. Therefore, conditions that stimulate carbon monoxide or $\cdot\text{NO}$ production can stimulate H_2S synthesis²³.

Low steady-state tissue H_2S concentrations²⁴ result primarily from the high activity of the mitochondrial sulfide oxidation pathway²⁵. Sulfide quinone oxidoreductase (SQOR) commits H_2S to oxidation (Fig. 1a) while concomitantly reducing coenzyme Q (CoQ), which enters the electron transport chain (ETC) at the level of complex III. In addition to shielding cells from respiratory poisoning²⁶, SQOR modulates electron flux in the ETC, causing a reductive shift in the mitochondrial NAD^+ and CoQ pools²⁷, activating aerobic glycolysis^{28,29} and glutamine-dependent lipid synthesis³⁰. Interestingly, the proangiogenic effect of H_2S is reportedly mediated in part by ETC inhibition and enhanced aerobic glycolysis¹⁰. Although endothelial cells can meet up to 85% of their ATP needs from glycolysis³¹, complex III ablation decreases proliferation and angiogenesis and is associated with decreased amino acid levels³².

At H_2S concentrations that inhibit forward electron transfer, cells prioritize its clearance by rerouting electrons through complex II using fumarate as a terminal electron acceptor³³. A similar remodeling of the ETC via fumarate-dependent complex II reversal is observed in hypoxia³⁴. Sulfide oxidation by SQOR protects against hypoxia-induced injury in the brain, which is particularly vulnerable to O_2 deprivation³⁵. On the other hand, SQOR inhibition reportedly protects against heart failure in a mouse model³⁶. A deeper understanding of the role of SQOR in modulating vascular function is needed.

In the present study, we demonstrate that hypoxic upregulation of $\cdot\text{NO}$ synthesis in endothelial cells reprograms the transsulfuration pathway to increase γ -CTH-dependent H_2S biogenesis. The proangiogenic effects of H_2S depend on its oxidative metabolism; SQOR deficiency decreases cell proliferation, sprouting capacity and tube formation in hypoxic endothelial cells. Whole-body and endothelial-specific *Sqor*-knockout (KO) mice showed diminished tumor growth and angiogenesis in a xenograft model. Consistent with these data, whole-body *Sqor*-KO mice also demonstrated decreased muscle angiogenesis in a hind limb ischemia model induced via femoral artery ligation. This study identifies SQOR as a therapeutic target for inhibiting the proangiogenic effects of H_2S under hypoxia for restricting tumor growth while also highlighting its importance for vascular regrowth following an ischemic event.

Results

Hypoxia stimulates H_2S biogenesis

Metabolomics analysis revealed decreased GSH in transformed (EA.hy926 and human dermal microvascular endothelial cell-1 (HMEC-1)) and primary (human umbilical vein endothelial cell (HUVEC)) endothelial cells cultured under hypoxic (2% O_2) versus normoxic (21%) conditions (Fig. 1b–d and Supplementary Table 1), which has been reported in other cell types^{37,38}. To test our hypothesis that hypoxia redirects cysteine away from GSH and toward H_2S synthesis, radiolabel transfer from [³⁵S]methionine to GSH was monitored (Fig. 1a). Hypoxia decreased the magnitude of radiolabel incorporation as well as the GSH pool size in all three endothelial cell lines (Fig. 1e–j). Extracellular thiosulfate, a stable biomarker of H_2S metabolism, increased under hypoxia (Fig. 1k–m), and increased radiolabel transfer from [³⁵S]methionine to thiosulfate was observed under these conditions (Fig. 1n). Three of four nonendothelial cell lines tested (HEK293, 143B and HepG2) also exhibited decreased radiolabel transfer and lower GSH pool size (Supplementary Fig. 1a–c,e–g), whereas significant differences were not observed in SH-SY5Y cells (Supplementary Fig. 1d,h). Hypoxic thiosulfate accumulation was only seen in HepG2 cells (Supplementary Fig. 1i–l), revealing that decreased flux to GSH is not necessarily coupled to increased H_2S metabolism under hypoxia.

Glutathione disulfide (GSSG) levels decreased across endothelial cell lines, indicating that lower GSH under hypoxia was not associated with oxidative stress (Supplementary Fig. 1m–o). Total (GSH + GSSG) glutathione was decreased in endothelial cells under hypoxia (Supplementary Fig. 2a–c). The complex vascular cell basal medium used for HUVEC culture suppressed thiosulfate accumulation and GSH labeling, although a diminution in the GSH pool was still observed (Supplementary Fig. 2d–f). The vascular cell basal medium also suppressed hypoxic thiosulfate accumulation by EA.hy926 cells, suggesting that growth factors influence H_2S homeostasis (Supplementary Fig. 2g). Regulation of CBS by nutrients and basic fibroblast growth factor has been reported previously³⁹.

$\cdot\text{NO}$ regulates hypoxic H_2S homeostasis

Hypoxia increases endothelial nitric oxide synthase (eNOS) activity and $\cdot\text{NO}$ production^{40–43}. We therefore posited that $\cdot\text{NO}$ would indirectly induce H_2S synthesis by γ -CTH (Fig. 2a). DETA NONOate, an $\cdot\text{NO}$ donor, elicited a dose-dependent increase in extracellular thiosulfate, whereas cPTIO, an $\cdot\text{NO}$ scavenger, decreased thiosulfate accumulation under normoxia (Fig. 2b,c). Cystathionine, used to competitively inhibit H_2S synthesis by γ -CTH, decreased hypoxic thiosulfate accumulation (Fig. 2d), whereas arginine, a substrate for $\cdot\text{NO}$ synthesis, had no effect (Supplementary Fig. 3a). Cystathionine supplementation did not change intracellular cysteine concentrations (Supplementary Fig. 3b). Cystine and homocystine, which upon intracellular reduction to cysteine and homocysteine, respectively, are substrates for H_2S synthesis, increased extracellular thiosulfate under normoxia (Fig. 2e,f). Importantly, the disulfides can also be converted to their respective persulfides (that is, cysteine persulfide and homocysteine persulfide) by the transsulfuration enzymes^{44,45} and release H_2S following reduction by thioredoxin⁴⁶. EA.hy926 (scrambled control) cells consumed extracellular cystine more rapidly at 8 h under hypoxia than under normoxia (Fig. 2g). By contrast, partial knockdown (KD) of *NOS3* or the upstream regulators *HIF1A* and *HIF2-alpha* (Supplementary Fig. 3c–h) decreased hypoxic thiosulfate accumulation (Fig. 2h,i), whereas roxadustat (FG4592), which stabilizes HIF, increased thiosulfate accumulation under normoxia (Supplementary Fig. 3i). Hypoxic HIF-1 α levels were not impacted by *Sqor* KD (Supplementary Fig. 3j,k). A small but significant increase in hypoxic GSH levels was seen in *NOS3*-KD cells (Fig. 2j).

SQOR promotes hypoxic endothelial cell proliferation

Deficiency of SQOR, but not persulfide dioxygenase (ETHE1; Supplementary Fig. 4a,b,d,e), attenuated EA.hy936 cell proliferation, which was profoundly exacerbated under hypoxia (Fig. 3a,b). SQOR deficiency in a second endothelial cell line, HMEC-1, also lowered cell proliferation (Supplementary Fig. 4c,f,g). The vasculogenic potential for forming capillary-like structures, as monitored by a tube formation assay, revealed that *SQOR*-KD cells were defective under both normoxic and hypoxic conditions (Fig. 3c,d and Supplementary Fig. 4h,i). *SQOR* KD in EA.hy926 and HMEC-1 cells diminished colony formation (Supplementary Fig. 4j–m). EA.hy926 spheroids with *SQOR*-KD cells had shorter sprout length (Fig. 3e,f) and lower sprout number (tip cells) under normoxic and hypoxic conditions (Supplementary Fig. 4n) than scrambled cells. By contrast, significant differences were not induced by ETHE1 deficiency. Although EdU⁺ cells tended to be lower in *SQOR*-KD cells than in scrambled control cells, the difference did not rise to statistical significance (Supplementary Fig. 4o). These data reveal that SQOR deficiency causes defective endothelial cell migration and proliferation. VEGF-induced endothelial cell angiogenic sprouting was assessed with a microphysiologic platform⁴⁷ and revealed significantly lower tip cell formation and cell proliferation in *SQOR*-KD cells under normoxic conditions (Supplementary Fig. 4p–r). These data suggest that SQOR deficiency compromises VEGF-induced angiogenic sprouting in endothelial cells. Previous studies in other cell types have

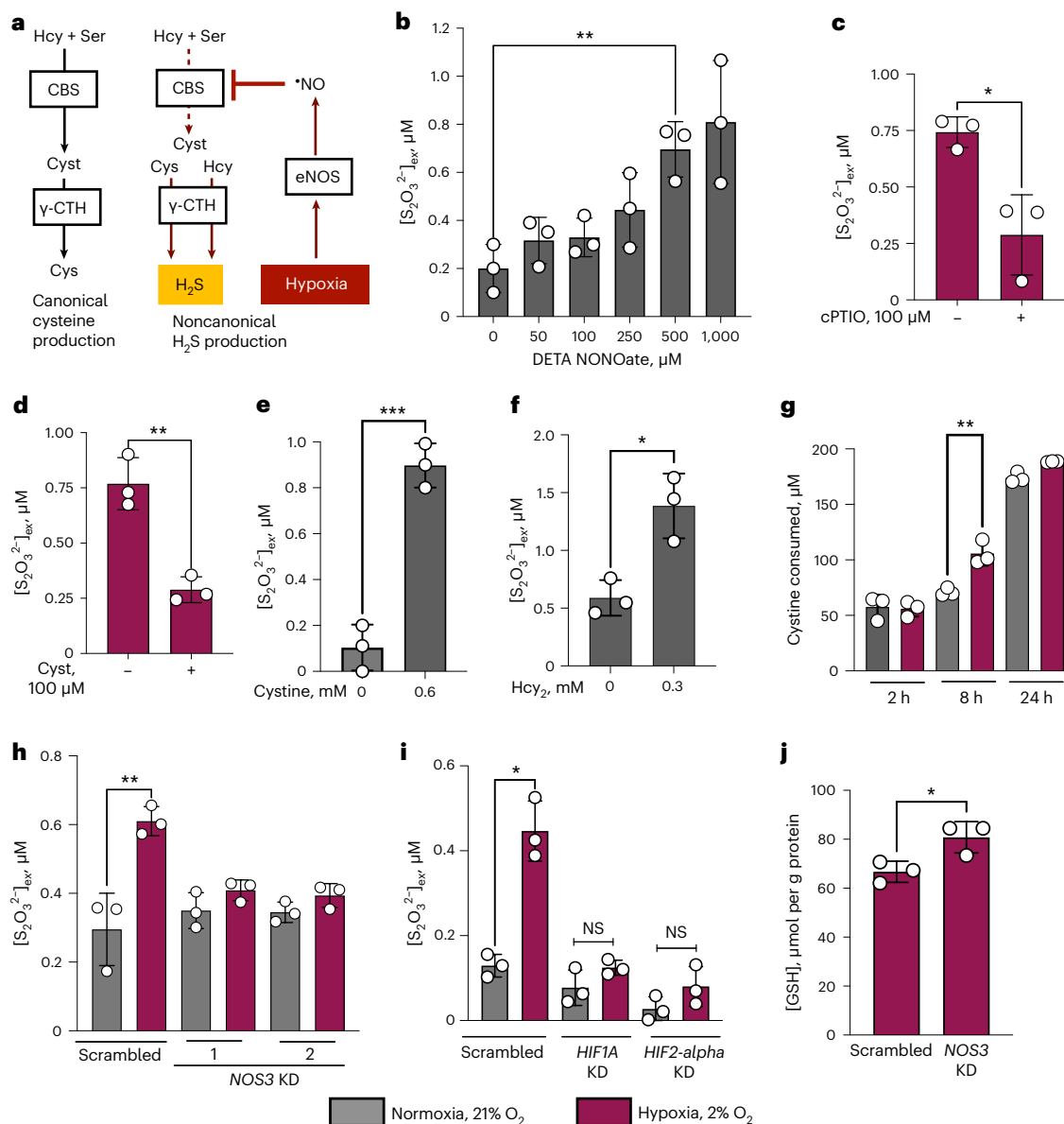


Fig. 2 | Intersection of ·NO and HIF signaling in hypoxic regulation of H₂S homeostasis. a, Scheme showing ·NO-induced switching at γ-CTH from cysteine (left) to H₂S synthesis (right). The broken arrow indicates lower flux through CBS, which promotes substrate and reaction specificity switching at γ-CTH under hypoxia (maroon); Ser, serine. **b**, Concentration dependence of extracellular thiosulfate ([S₂O₃²⁻]_{ex}) accumulation on DETA NONOate in EA.hy926 cells under normoxia (4 h, n = 3, **P = 0.005). **c, d**, Quantitation of hypoxic thiosulfate accumulation after 24 h in the presence of the ·NO scavenger cPTIO (**c**; n = 3, *P = 0.014) and cystathionine (**d**; n = 3, **P = 0.003). **e, f**, Changes in extracellular thiosulfate in EA.hy926 cells in the presence of cystine (**e**) and

homocystine (**f**) at 24 h (n = 3, ***P = 0.0006 and *P = 0.013). Hcy₂, homocystine. **g**, Cystine consumption by EA.hy926 scrambled controls cells under hypoxia (n = 3, **P = 0.006). **h**, KD of *NOS3* (using short hairpin RNA (shRNA) sequences 1 and 2, n = 3, **P = 0.008) lowered extracellular thiosulfate. **i**, Impact of *HIF1A* or *HIF2-alpha* (n = 3, *P = 0.010) KD in EA.hy926 cells on hypoxic extracellular thiosulfate accumulation at 24 h; NS, not significant. **j**, Impact of *NOS3* KD in EA.hy926 cells on hypoxic intracellular GSH concentration ([GSH]_{in}) after 24 h (n = 3, *P = 0.034). Data represent mean values ± s.d. in **b–j**; statistics were derived from unpaired two-sided Student's *t*-tests. *n* denotes the number of independent experiments.

reported a hypoxic increase in intracellular GSSG levels³⁷. The lower GSH and GSSG levels under hypoxic conditions across scrambled, *SQOR*- and *ETHE1*-KD EA.hy926 cells (Fig. 3g–i) indicates that an oxidative stress mechanism is unlikely to be associated with the *SQOR* deficiency-induced proliferation defect.

Mitochondrial reductive shifts restrict cell proliferation

SQOR deficiency is predicted to impair H₂S oxidation, which was confirmed by the reduced rate of H₂S clearance and thiosulfate accumulation by *SQOR* KD versus scrambled controls (Fig. 4a, b). The expected 2:1 stoichiometry between H₂S consumed and thiosulfate produced was seen in control cells but not in *SQOR*-KD cells (Fig. 4c), where

thiosulfate levels were comparable to background levels. Due to its volatility, a sizeable abiotic loss of H₂S was seen even in the absence of cells. Additionally, hypoxic extracellular thiosulfate accumulation was not observed in *SQOR*-KD cells in contrast to scrambled control cells (Fig. 4d).

SQOR-KD cells exhibited increased glucose consumption under hypoxia, which was paralleled by extracellular lactate accumulation (Fig. 4e, f). An earlier study reported *K*_{ATP} channel activation as a mechanism of H₂S regulation of endothelial cell proliferation⁹. However, neither the *K*_{ATP} channel activator SG-209 nor the channel blocker glybenclamide affected proliferation of scrambled or *SQOR*-KD EA.hy926 or HMEC-1 cells (Supplementary Fig. 5a, b). H₂S targets complex IV and blocks

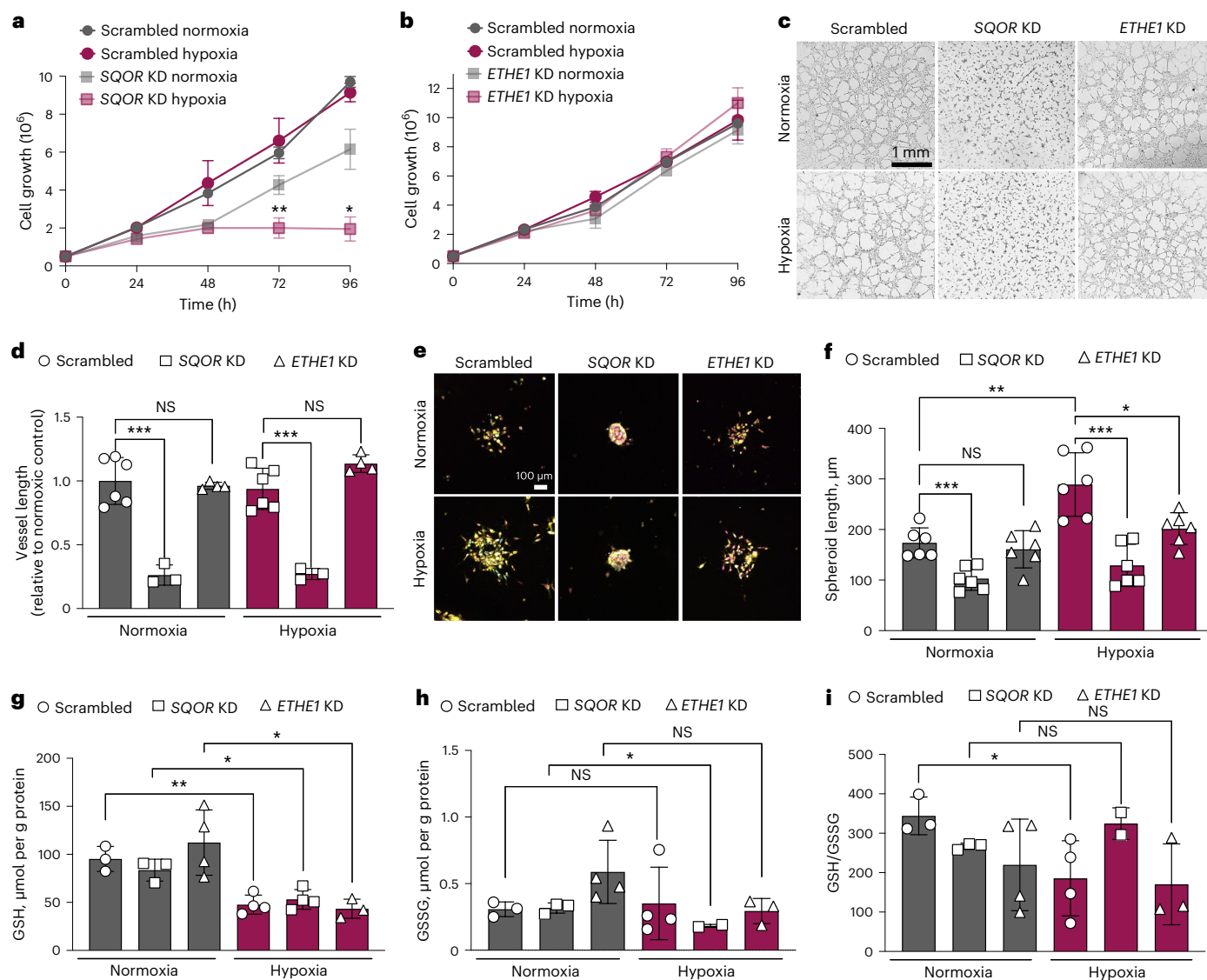


Fig. 3 | SQOR deficiency decreases endothelial cell proliferation via a nonoxidative stress mechanism. a, b, Differences in proliferation of SQOR-KD (**a**; $n = 3$, $*P = 0.047$, $**P = 0.0056$) versus ETHE1-KD (**b**; $n = 3$) EA.hy926 cells and scrambled control cells under normoxic and hypoxic conditions. **c, d**, Effects of SQOR KD on tube formation (**c**). Defects are evidenced by differences in vessel length (**d**); $n = 6$ (scrambled), $n = 3$ (SQOR KD) and $n = 4$ (ETHE1 KD); $***P = 0.0003$ in both normoxia and hypoxia. **e, f**, Representative images of EA.hy926 cells (scrambled, SQOR KD and ETHE1 KD) in a spheroid sprouting assay. **e**, The images show the overlay of DAPI, Edu and Ulex Europaeus agglutinin-1 (UEA) staining, as described in the Methods. **f**, Quantitation of spheroid length from the center

to the longest sprout is shown; $n = 6$ independent spheroids; $**P = 0.0023$ (scrambled in normoxia versus hypoxia), $***P = 0.001$ (normoxia) and $*P = 0.012$ and $***P = 0.0004$ (hypoxia). **g–i**, Quantitation of GSH ($n = 3$ or 4 as indicated by the number of data points; $**P = 0.0026$ and $*P = 0.0130$ (SQOR KD) and $*P < 0.0027$ (ETHE1 KD); **g**), GSSG ($*P = 0.012$; **h**) and GSH/GSSG ($*P = 0.049$; **i**) in the indicated EA.hy926 cells ($n = 2, 3$ or 4 as indicated by the number of data points in **h** and **i**). Data in **g–i** are from four independent experiments ($n = 4$), and each dot represents an individual sample. Data represent mean values \pm s.d. in **a, b, d, f–i**, and statistics were derived from unpaired two-sided Student's *t*-tests.

forward electron transfer, which is expected to lower the NAD⁺:NADH ratio. SQOR deficiency induced a reductive shift in EA.hy926 cells, as seen previously in HT29 cells²⁶, which was exacerbated under hypoxia (Fig. 4g). An unbiased metabolomics analysis of EA.hy926 cells revealed accumulation of glycerol-3-phosphate (G3P), L-2-hydroxyglutarate and N-carbamoyl aspartate under normoxic conditions (Fig. 4h and Supplementary Table 2). These changes are consistent with an SQOR deficiency-induced reductive shift in the mitochondrial pyridine nucleotide pool, as previously seen in H₂S-treated cells²⁶. Surprisingly, however, L-2-hydroxyglutarate and N-carbamoyl aspartate decreased under hypoxia in SQOR-KD cells (Fig. 4i and Supplementary Table 2).

We evaluated the role of reductive stress in growth impairment associated with SQOR deficiency by supplementing with the electron acceptor pyruvate or by expression of mito-LbNOX, a water-forming

NADH oxidase from *Lactobacillus brevis* targeted to the mitochondrion⁴⁸ (Supplementary Fig. 5c). Both interventions promoted proliferation of SQOR-KD cells (Fig. 4j, k). These data support the model that hypoxic activation of H₂S synthesis requires support of SQOR activity to avert complex IV inhibition and ETC backup, thereby activating glycolysis for ATP generation and diverting the tricarboxylic acid (TCA) cycle for macromolecular precursor synthesis (Fig. 4l). The physiological relevance of SQOR in neoangiogenesis was tested next in animal model studies, as described below.

SQOR deficiency decreases postischemia muscle angiogenesis Femoral artery ligation induces ischemia and promotes angiogenesis in the distal part of the limb and especially in the gastrocnemius muscles. Surgery was performed 2 weeks after tamoxifen injection (Fig. 5a).

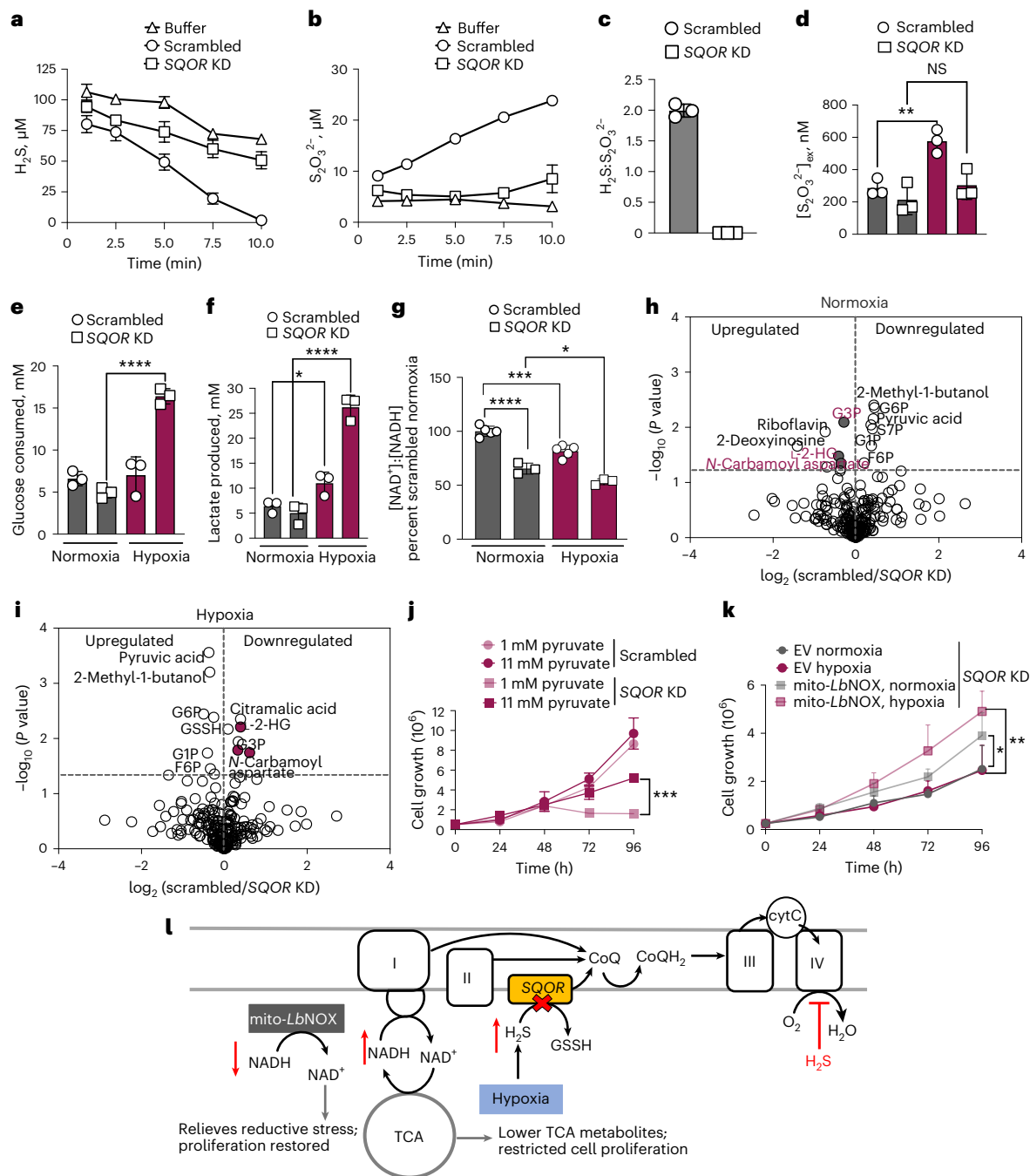


Fig. 4 | SQOR deficiency induces a reductive shift in the mitochondrial NADH pool. a–c, The kinetics of H₂S consumption (**a**) and intracellular thiosulfate production (**b**) by EA.hy926 cells in suspension (10% wt/vol), 21% O₂) revealed a 2:1 H₂S:S₂O₃²⁻ ratio for scrambled, but not SQOR-KD, cells (**c**; $n = 3$ in **a–c**). **d**, Comparison of extracellular thiosulfate levels after 24 h of culture of scrambled and SQOR-KD EA.hy926 cells in 2% versus 21% O₂ (** $P = 0.0051$, $n = 3$). **e, f**, Comparison of glucose consumption ($n = 3$, **** $P < 0.0001$; **e**) and lactate production ($n = 3$, * $P = 0.0345$ and **** $P < 0.0001$; **f**) by EA.hy926 cells after 48 h in 2% versus 21% O₂. **g**, Quantitation of the NAD⁺:NADH ratio in SQOR-KD versus scrambled EA.hy926 cells after 24 h in 2% versus 21% O₂ ($n = 5$ for scrambled and $n = 3$ for SQOR-KD; * $P = 0.0218$, **** $P = 0.0005$ and **** $P < 0.0001$). **h, i**, Metabolomics data reveal differential regulation of NADH-sensitive metabolites under normoxic (**h**) and hypoxic (**i**) conditions in SQOR-KD cells

($n = 4$). The horizontal lines in **h** and **i** represent a P value of 0.05, which was derived from a two-sample t -test with unequal variance; each metabolite is represented as the ratio of mean values on a log₂ scale; G6P, glucose-6-phosphate; G1P, glucose-1-phosphate; S7P, sedoheptulose-7-phosphate; L-2-HG, L-2-hydroxyglutarate. **j, k**, Effect of pyruvate supplementation under hypoxic conditions ($n = 3$, *** $P = 0.0003$; **j**) or expression of mito-LbNOX ($n = 3$, each in duplicate, * $P = 0.030$ and *** $P = 0.0012$; **k**) on growth restriction in SQOR-KD EA.hy926 cells under normoxic and hypoxic conditions. EV, empty vector. The slower growth kinetics in **k** could be due to doxycycline added to induce mito-LbNOX expression. **l**, Model explaining how SQOR-KD exacerbates reductive stress due to increased hypoxic H₂S synthesis, which can be alleviated by dissipating NADH levels. Data represent mean \pm s.d. in **a–g** and **j–k**, and statistics were derived from unpaired two-sided Student's t -tests; cytC, cytochrome c.

Whole-body Cre recombinase expression (WB^{Cre}) was induced by daily intraperitoneal tamoxifen injections for 5 days and was validated in the colon and liver by western blotting and assessment of the concentration

of urinary thiosulfate, a marker of H₂S oxidation, 10 days after tamoxifen injection (Fig. 5b–f). Blood flow was similarly impaired in both *Sqor*^{fl/fl} and WB^{Cre}*Sqor*^{fl/fl} mice on day 1 after surgery. Neovascularization, which

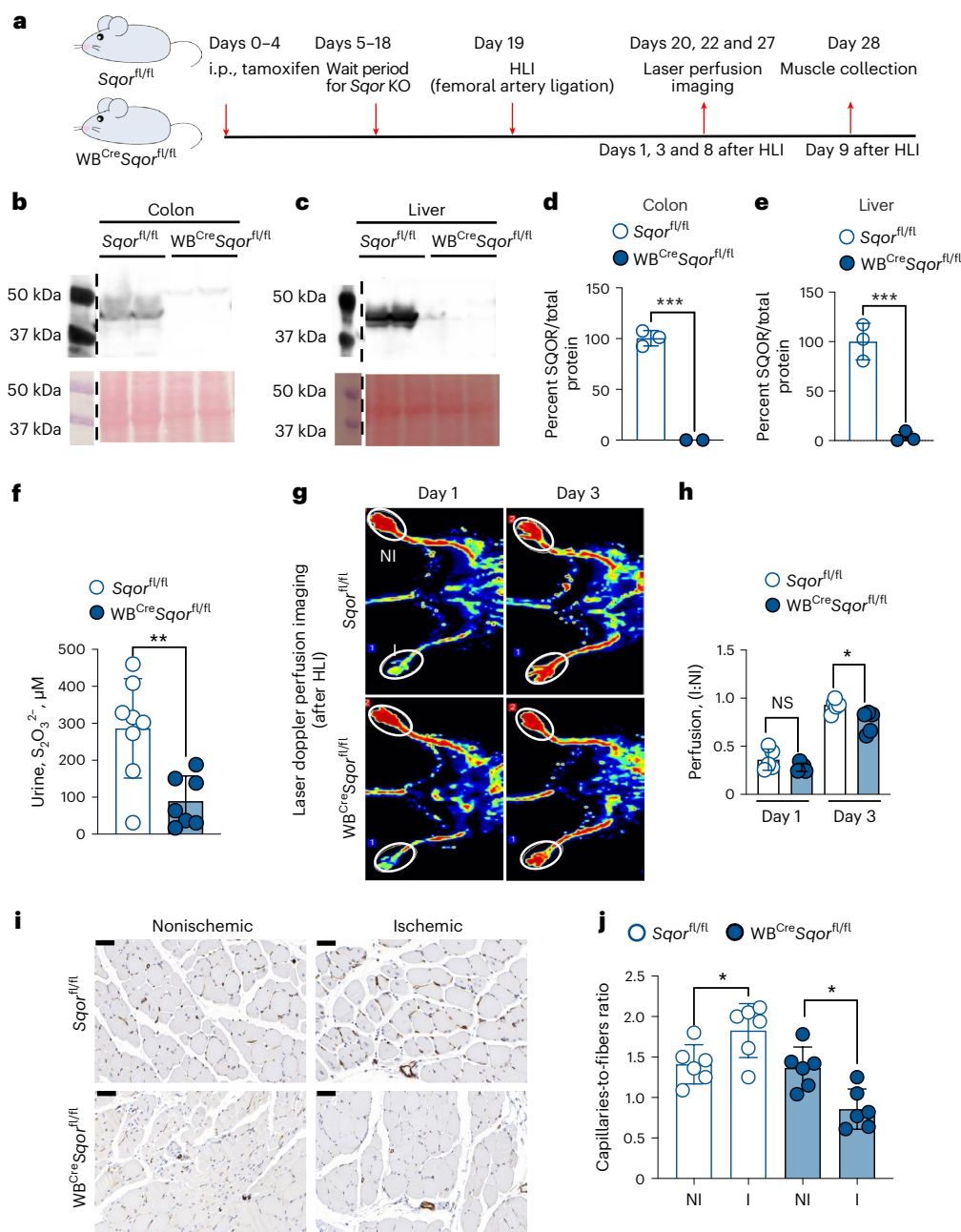


Fig. 5 | *Sqor* KO decreases angiogenesis in a hind limb ischemia model.

a, Experimental design for the induction of hind limb ischemia (HLI) by femoral artery ligation in *WB^{Cre}Sqor^{fl/fl}* versus *Sqor^{fl/fl}* mice; i.p., intraperitoneal. **b–e**, Representative western blot data and quantitation of SQOR expression in the colon (**b** and **d**) and liver (**c** and **e**) of *WB^{Cre}Sqor^{fl/fl}* and *Sqor^{fl/fl}* mice (each lane in **b** and **c** and each symbol in **d** and **e** represent samples from a different mouse; ****P* < 0.0004). **f**, Urinary thiosulfate levels are lower in *WB^{Cre}Sqor^{fl/fl}* mice than in control mice (*n* = 8 for *Sqor^{fl/fl}* mice and *n* = 7 for *WB^{Cre}Sqor^{fl/fl}* mice; ***P* = 0.004). **g**, Laser Doppler perfusion imaging at days 1 and 3 after hind limb ischemia. The

white ovals outline the distal regions where angiogenesis is stimulated in the bottom ischemic limbs after surgery, but not in the top nonischemic limbs. **h**, Blood perfusion is plotted as the ratio of ischemic:nonischemic limb (I:NI; *n* = 5, **P* = 0.024). **i**, CD31 staining of gastrocnemius muscle collected on day 9 (from four independent animals); scale bars, 50 μm. **j**, Quantitation of CD31 staining as the ratio of capillaries to fibers from six different areas in four mice (**P* = 0.0325 (littermate control mice) and **P* = 0.0290 (KO mice)). Data represent mean ± s.d. in **d–f**, **h** and **j**, and statistics were derived from unpaired two-sided Student's *t*-tests.

is indicated by the return of blood flow monitored by Doppler flow imaging, was lower in *Sqor*-KO mice than in control mice on day 3 (Fig. 5g,h). On day 8, an ~16% lower ratio of ischemic:nonischemic blood perfusion was observed in *WB^{Cre}Sqor^{fl/fl}* mice, although the difference did not rise to statistical significance (Supplementary Fig. 6a,b). However, CD31 staining of gastrocnemius muscle on day 9 revealed lower capillary:muscle fiber ratios in *WB^{Cre}Sqor^{fl/fl}* mice than in *Sqor^{fl/fl}* mice (Fig. 5i,j). By contrast, histological examination of lung sections revealed no difference in CD31 staining (Supplementary Fig. 6c,d), indicating that blood vessel

maintenance was not impacted following the induction of SQOR deficiency at least over the time frame of the experiment. These results are consistent with the importance of SQOR during neovascularization.

SQOR deficiency restricts tumor growth and angiogenesis

We tested the impact of SQOR deficiency in a tumor xenograft model in which syngeneic YUMMS.2 mouse melanoma cells were transplanted subcutaneously in 8- to 10-week-old control *Sqor^{fl/fl}* and *WB^{Cre}Sqor^{fl/fl}* mice (Fig. 6a). As a control, we established that endothelial cell

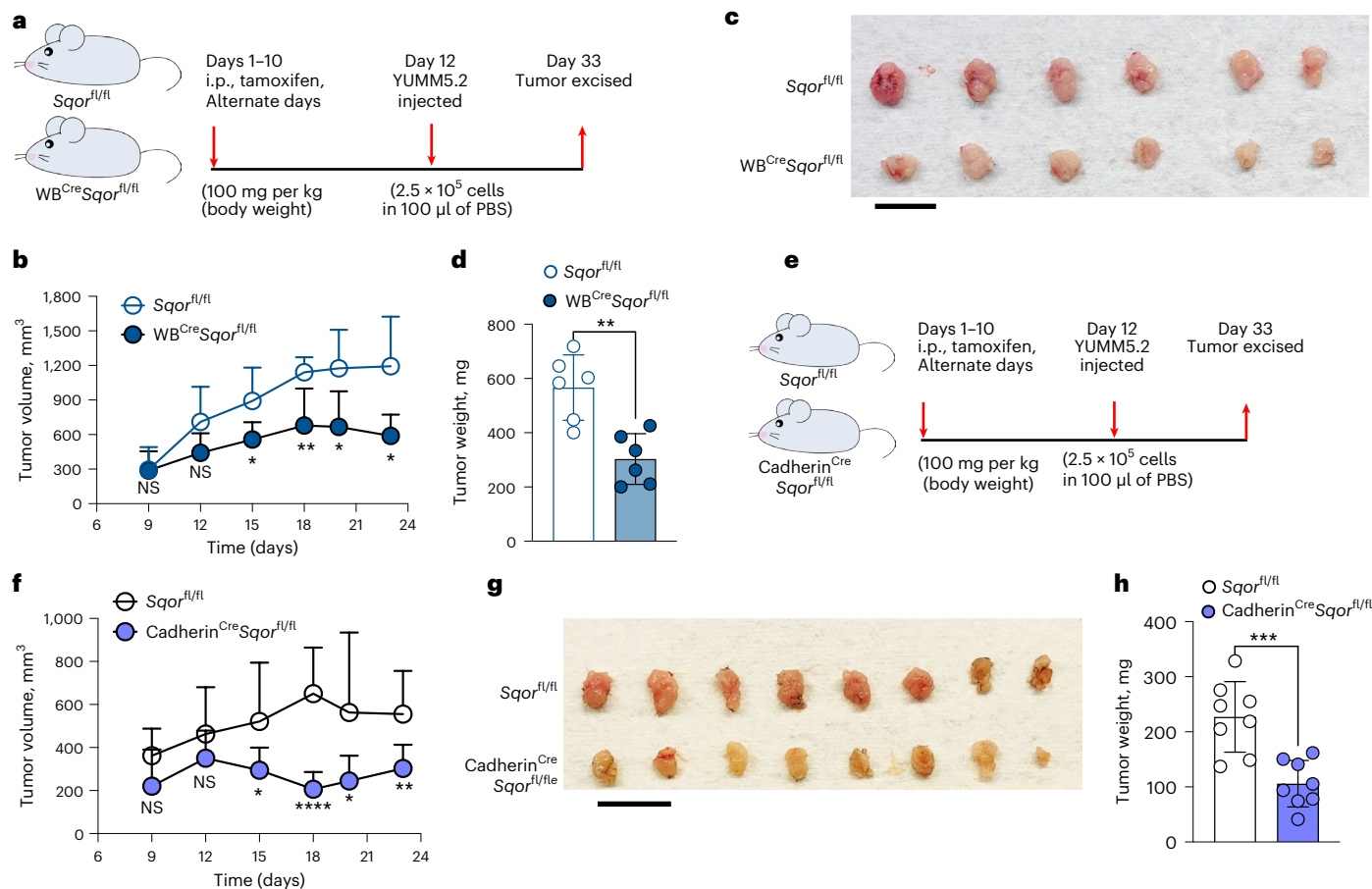


Fig. 6 | SQOR activity supports tumor growth and angiogenesis. **a–c**, Scheme showing induction of *Sgor* KO and syngeneic tumor generation in $WB^{Cre}Sgor^{fl/fl}$ mice (**a**), tumor volume (**b**) and tumor size at the end of the experiment (**c**; $n = 6$ in each group in **b** and **c**; $*P = 0.031$ (day 15), $**P = 0.009$ (day 18), $*P = 0.020$ (day 20) and $*P = 0.010$ (day 23)). **d**, Comparison of tumor mass in the two groups in **c** ($n = 6$, $**P = 0.0017$). **e**, Scheme showing the induction of *Sgor* KO and syngeneic

tumor generation in VE-cadherin $^{Cre-ERT2}Sgor^{fl/fl}$ mice. **f–h**, Comparison of tumor volume ($*P < 0.045$, $**P = 0.008$ and $****P < 0.0001$; **f**), tumor size after collection (**g**) and tumor mass (**h**) from VE-cadherin $^{Cre-ERT2}Sgor^{fl/fl}$ ($n = 8$) versus *Sgor* $^{fl/fl}$ ($n = 8$) mice ($***P = 0.005$). Data represent mean values \pm s.d. in **b**, **d**, **f** and **h**, and statistics were derived from unpaired two-sided Student's *t*-tests. Scale bars, 2 cm.

proliferation is not modulated by thiosulfate under hypoxic or normoxic conditions (Supplementary Fig. 7a–c). Tumors in $WB^{Cre}Sgor^{fl/fl}$ mice were significantly smaller than in *Sgor* $^{fl/fl}$ mice (Fig. 6b–d and Supplementary Fig. 7d,e) and exhibited markedly lower tumor Ki67 staining (Supplementary Fig. 7f,g). Immunohistochemical analysis of CD31, an endothelial marker, revealed significantly decreased vessel number (Supplementary Fig. 7h,i), consistent with the in vitro data (Fig. 3a–f).

We next examined the effect of endothelial-specific SQOR deficiency on tumor growth and angiogenesis. Endothelial-specific *Sgor* KO was confirmed by fluorescence-activated cell sorting (FACS) analysis of lung cells from VE-cadherin $^{Cre-ERT2}Sgor^{fl/fl}$ and littermate *Sgor* $^{fl/fl}$ control mice (Supplementary Fig. 7j–m). SQOR deficiency was observed in CD31 $^{+}$ endothelial cells but not in CD31 $^{+}$ CD45 $^{+}$ leukocyte cells (Supplementary Fig. 7n,o). By contrast, *ETHE1* expression was comparable in CD31 $^{+}$ and CD31 $^{+}$ CD45 $^{+}$ cell fractions (Supplementary Fig. 7p–q).

YUMM5.2 mouse melanoma cells were implanted subcutaneously in 8- to 10-week-old syngeneic mice (Fig. 6e). Tumor growth kinetics, assessed every 2–3 days, were significantly slower from day 15 in VE-cadherin $^{Cre-ERT2}Sgor^{fl/fl}$ mice than in control mice, and the endpoint tumor weight was lower on day 33 (Fig. 6f–h). Additionally, immunohistochemical analysis revealed lower Ki67 and CD31 staining in tumor sections from VE-cadherin $^{Cre-ERT2}Sgor^{fl/fl}$ mice (Supplementary Fig. 8a–d).

Discussion

Although the interdependence of \cdot NO and H₂S on vascular function is known, the molecular basis by which eNOS deficiency inhibits

H₂S-mediated neovascularization or how γ -CTH loss lowers sprout formation induced by the \cdot NO donor 2-(*N,N*-diethylamino)-diazolol-2-oxide has remained elusive⁸. In this study, we demonstrate that the hypoxic induction of eNOS disconnects metabolic flux between CBS and γ -CTH in the canonical transsulfuration pathway (Fig. 2a), decreases GSH synthesis and promotes H₂S metabolism. Hypoxic enhancement of extracellular cystine consumption as well as homocysteine accumulation due to CBS inhibition presumably provisions γ -CTH with the substrates for H₂S production. In this model, \cdot NO acts as an upstream regulator of H₂S biogenesis, promoting hypoxic H₂S synthesis instead of the canonical cysteine synthesis.

Previous studies linked the hypoxic lowering of GSH to increased reactive oxygen species^{37,38}. In this study, we saw lower GSSG in endothelial cells grown under hypoxic conditions (Supplementary Fig. 1m–o), suggesting an alternate mechanism for lowering GSH. We demonstrate that endothelial cells prioritize cysteine use for H₂S generation over GSH production, leading to a decreased GSH pool size. The oxidative pentose phosphate pathway is a major source of NADPH, and increased turnover of oxidized GSH by NADPH-dependent glutathione reductase might be involved in protecting against reactive oxygen species under hypoxia. In this context, inhibition of the oxidative pentose phosphate pathway has been shown to decrease HUVEC viability and impair blood vessel maturation^{49,50}.

The hypoxia–HIF axis regulates both tip cell migration and stalk cell proliferation through transcription of proangiogenic factors,

including VEGF and NOS⁵¹. Our results indicate that upregulation of H₂S metabolism lies downstream of HIF stabilization because *HIF1A*- and *HIF2-alpha*-KD cells under hypoxia decreased H₂S oxidation, whereas FG4592-treated cells under normoxia increased H₂S oxidation, as reported by the proxy marker thiosulfate (Fig. 2i and Supplementary Fig. 3i). Even highly glycolytic cells need a functional TCA cycle to generate macromolecular precursors, as evidenced by inhibition of endothelial cell proliferation by ablation of complex III^{32,52}. A balance between endothelial cell migration and proliferation is key to angiogenesis⁴⁷. Although the ETC inhibitors cyanide, phenformin and oligomycin stimulate migration¹⁰, H₂S oxidation also regulates proliferation (Fig. 3a). Furthermore, a role for H₂S, per se, rather than the glutathione persulfide product of SQOR in regulating proliferation is indicated by the absence of an observable effect in *ETHE1*-KD cells (Fig. 3b). Because *ETHE1* oxidizes glutathione persulfide to sulfite⁵³ (Fig. 1a), this reactive low-molecular-weight persulfide accumulates in *ETHE1*-KD cells, triggering the formation of additional poly- and persulfide derivatives⁴⁵, which can be additional sources of H₂S following reduction, for example, by thioredoxin⁴⁶. We posit that H₂S exerts its proangiogenic effect by stimulating SQOR activity and inhibiting complex IV, which shifts energy metabolism from oxidative phosphorylation toward aerobic glycolysis^{10,28,31}. This shift would support rapid ATP production to meet the energy demands of motile tip cells.

The efficiency of the sulfide oxidation machinery is important for maintaining very low steady-state levels of sulfide^{26,54}. A spike in endogenous H₂S levels^{12,35} could synergize with hypoxia to dampen ETC flux by increasing the K_m for O₂ of cytochrome *c* oxidase, which is very low (<0.2 to 1 μM, corresponding to <0.02–0.1% O₂ tension)^{27,55}. Thus, even in the colon where the estimated O₂ tension is as low as 0.4%, the O₂ concentration is 4- to 20-fold higher than the K_m for cytochrome *c* oxidase, which should be insensitive to hypoxic regulation in the absence of additional modulation⁵⁶. Our study helps explain this apparent paradox by demonstrating that although endothelial cells proliferate equally well under normoxic and hypoxic conditions, SQOR deficiency drastically reduces proliferation, particularly under hypoxia (Fig. 3a and Supplementary Fig. 4g). We interpret these data as evidence for a steady-state increase in H₂S levels due to SQOR deficiency with a concomitant and sustained inhibition of the ETC ($K_{i(H_2S)} \approx 200$ nM (ref. 57)), which, in turn, induces reductive stress and limits TCA cycle activity, inhibiting proliferation (Fig. 4i). Consistent with this model, SQOR-deficient endothelial cells grown under normoxic conditions accumulate higher levels of 2-hydroxyglutarate (Fig. 4h; a product of α-ketoglutarate reduction and a marker of ETC dysfunction) than scrambled control cells^{58,59}. Additionally, levels of G3P and *N*-carbamoyl aspartate also increase under these conditions. G3P shuttles reducing equivalents generated by cytosolic G3P dehydrogenase during the NADH-dependent oxidation of dihydroxyacetone phosphate. The mitochondrial isoform of the same enzyme then transfers electrons transiently to FAD as it catalyzes the oxidation of G3P to dihydroacetone phosphate and uses CoQ as the final electron acceptor. *N*-Carbamoyl aspartate is a precursor of dihydroorotate in the pyrimidine biosynthesis pathway. Accumulation of G3P and carbamoyl phosphate is consistent with a reductive shift in the ETC, which is further supported by the significantly higher NAD⁺:NADH ratio in SQOR-deficient cells (Fig. 4g). Surprisingly, lower levels of L-hydroxyglutarate, G3P and carbamoyl aspartate were seen in *SQOR*-KD cells grown under hypoxic conditions (Fig. 4i), suggesting a more complex interplay between SQOR deficiency and hypoxia, which warrants further investigation. We speculate that metabolism of L-hydroxyglutarate to the corresponding lactone might be promoted in *SQOR*-KD cells grown under hypoxic conditions due to lactate accumulation and a concomitant decrease in pH⁶⁰. Similarly, the ATP-dependent synthesis of carbamoyl aspartate might be decreased in *SQOR*-KD cells grown under hypoxic conditions. Thus, although H₂S modulates the cellular response to hypoxia in endothelial cells, its sustained accumulation in SQOR-deficient cells is

detrimental for proliferation due to complex metabolic changes and is consistent with the reported antiproliferative effect of reductive stress that is cell specific⁶¹.

The physiological relevance of SQOR in angiogenesis is exemplified by decreased tumor angiogenesis in whole-body and endothelial-specific *Sqor*-KO mice, suggesting that H₂S build up due to induction of intratumoral H₂S synthesis in the hypoxic tumor microenvironment is sufficient to restrict tumor growth. Our findings are consistent with a recent report that demonstrated that dietary methionine supplementation to boost H₂S reduces tumor progression via stimulation of antitumor immunity⁶². Similarly, in the femoral ligation model for hind limb ischemia, whole-body *Sqor*-KO mice demonstrated reduced blood flow as well as decreased muscle angiogenesis compared to control mice. A previous *in vitro* study on *Sqor* KD in Hepa 1-6 cells identified a protective role for H₂S oxidation in ischemia/reperfusion injury⁶³. Other studies using mouse SQOR deficiency models induced either by global *Sqor* KO or mislocalization via deletion of the mitochondrial leader sequence reported that homozygous *Sqor*^{-/-} pups failed to thrive and did not survive past 8 or 10 weeks of birth^{35,64}. The effect of SQOR deficiency on the development of blood vessels was not evaluated in these studies. In our study, whole-body and endothelial-specific *Sqor* KO was induced -2 months after birth. The absence of an effect on lung CD31 expression indicates that SQOR is not required for blood vessel maintenance at least over the duration of our study (Supplementary Fig. 6c,d). Our model thus allowed for the evaluation of the effects of SQOR deficiency on neovascularization in pathological contexts in adult mice.

The interdependence of O₂ and H₂S metabolism in ETC flux has significant physiological relevance as evidenced by the sensitivity of the brain to ischemia due to low levels of SQOR³⁵, further demonstrating that low H₂S clearance capacity represents a metabolic vulnerability. We have previously demonstrated that sustained inhibition of the ETC by H₂S leads to recruitment of a redox cycle between SQOR and complex II, which prioritizes H₂S removal and CoQ regeneration, using fumarate as a terminal electron acceptor³³. Although hypoxia also leads to utilization of fumarate as a terminal electron acceptor in multiple tissues³⁴, the contribution of this redox cycle in endothelial cells and its modulation by H₂S remain to be assessed.

In summary, we demonstrate that hypoxic reprogramming of the transsulfuration pathway by ·NO induces H₂S in endothelial cells and is critical for angiogenesis. This study revealed the underlying mechanism by which ·NO, H₂S and O₂ metabolism intersect to regulate ETC redox state and angiogenesis. Finally, our study revealed a key role for sulfide oxidation rather than reactive persulfide species in angiogenesis and nominated SQOR as a rational drug target for antiangiogenesis therapy in different disease settings.

Online content

Any methods, additional references, Nature Portfolio reporting summaries, source data, extended data, supplementary information, acknowledgements, peer review information; details of author contributions and competing interests; and statements of data and code availability are available at <https://doi.org/10.1038/s41589-024-01583-8>.

References

1. Carmeliet, P. Angiogenesis in health and disease. *Nat. Med.* **9**, 653–660 (2003).
2. Carmeliet, P. Angiogenesis in life, disease and medicine. *Nature* **438**, 932–936 (2005).
3. Folkman, J. Angiogenesis. *Annu. Rev. Med.* **57**, 1–18 (2006).
4. Hurwitz, H. et al. Bevacizumab plus irinotecan, fluorouracil, and leucovorin for metastatic colorectal cancer. *N. Engl. J. Med.* **350**, 2335–2342 (2004).
5. Ribatti, D., Annesse, T., Ruggieri, S., Tamma, R. & Crivellato, E. Limitations of anti-angiogenic treatment of tumors. *Transl. Oncol.* **12**, 981–986 (2019).

6. Szabo, C. & Papapetropoulos, A. Hydrogen sulphide and angiogenesis: mechanisms and applications. *Br. J. Pharmacol.* **164**, 853–865 (2011).
7. Rushing, A. M. et al. Effects of a novel hydrogen sulfide prodrug in a porcine model of acute limb ischemia. *J. Vasc. Surg.* **69**, 1924–1935 (2019).
8. Coletta, C. et al. Hydrogen sulfide and nitric oxide are mutually dependent in the regulation of angiogenesis and endothelium-dependent vasorelaxation. *Proc. Natl Acad. Sci. USA* **109**, 9161–9166 (2012).
9. Papapetropoulos, A. et al. Hydrogen sulfide is an endogenous stimulator of angiogenesis. *Proc. Natl Acad. Sci. USA* **106**, 21972–21977 (2009).
10. Longchamp, A. et al. Amino acid restriction triggers angiogenesis via GCN2/ATF4 regulation of VEGF and H₂S production. *Cell* **173**, 117–129 (2018).
11. Olson, K. R. et al. Hydrogen sulfide as an oxygen sensor/transducer in vertebrate hypoxic vasoconstriction and hypoxic vasodilation. *J. Exp. Biol.* **209**, 4011–4023 (2006).
12. Morikawa, T. et al. Hypoxic regulation of the cerebral microcirculation is mediated by a carbon monoxide-sensitive hydrogen sulfide pathway. *Proc. Natl Acad. Sci. USA* **109**, 1293–1298 (2012).
13. Singh, S. & Banerjee, R. PLP-dependent H₂S biogenesis. *Biochim. Biophys. Acta* **1814**, 1518–1527 (2011).
14. Zou, C.-G. & Banerjee, R. Homocysteine and redox signaling. *Antioxid. Redox Signal.* **7**, 547–559 (2005).
15. Vitvitsky, V. et al. Perturbations in homocysteine-linked redox homeostasis in a murine model for hyperhomocysteinemia. *Am. J. Physiol. Regul. Integr. Comp. Physiol.* **287**, R39–R46 (2004).
16. Kumar, R. & Banerjee, R. Regulation of the redox metabolome and thiol proteome by hydrogen sulfide. *Crit. Rev. Biochem. Mol. Biol.* **56**, 221–235 (2021).
17. Hanna, D., Kumar, R. & Banerjee, R. A metabolic paradigm for hydrogen sulfide signaling via electron transport chain plasticity. *Antioxid. Redox Signal.* **38**, 57–67 (2023).
18. Banerjee, R. Catalytic promiscuity and heme-dependent redox regulation of H₂S synthesis. *Curr. Opin. Chem. Biol.* **37**, 115–121 (2017).
19. Kozich, V. et al. Human ultrarare genetic disorders of sulfur metabolism demonstrate redundancies in H₂S homeostasis. *Redox Biol.* **58**, 102517 (2022).
20. Chiku, T. et al. H₂S biogenesis by human cystathionine γ-lyase leads to the novel sulfur metabolites lanthionine and homolanthionine and is responsive to the grade of hyperhomocysteinemia. *J. Biol. Chem.* **284**, 11601–11612 (2009).
21. Weeks, C. L., Singh, S., Madzelan, P., Banerjee, R. & Spiro, T. G. Heme regulation of human cystathionine β-synthase activity: insights from fluorescence and Raman spectroscopy. *J. Am. Chem. Soc.* **131**, 12809–12816 (2009).
22. Singh, S., Madzelan, P. & Banerjee, R. Properties of an unusual heme cofactor in PLP-dependent cystathionine β-synthase. *Nat. Prod. Rep.* **24**, 631–639 (2007).
23. Kabil, O., Yadav, V. & Banerjee, R. Heme-dependent metabolite switching regulates H₂S synthesis in response to ER stress. *J. Biol. Chem.* **291**, 16418–16423 (2016).
24. Furne, J., Saeed, A. & Levitt, M. D. Whole tissue hydrogen sulfide concentrations are orders of magnitude lower than presently accepted values. *Am. J. Physiol. Regul. Integr. Comp. Physiol.* **295**, R1479–R1485 (2008).
25. Vitvitsky, V., Kabil, O. & Banerjee, R. High turnover rates for hydrogen sulfide allow for rapid regulation of its tissue concentrations. *Antioxid. Redox Signal.* **17**, 22–31 (2012).
26. Libiad, M. et al. Hydrogen sulfide perturbs mitochondrial bioenergetics and triggers metabolic reprogramming in colon cells. *J. Biol. Chem.* **294**, 12077–12090 (2019).
27. Banerjee, R. & Kumar, R. Gas regulation of complex II reversal via electron shunting to fumarate in the mammalian ETC. *Trends Biochem. Sci.* **47**, 689–698 (2022).
28. Vitvitsky, V. et al. The mitochondrial NADH pool is involved in hydrogen sulfide signaling and stimulation of aerobic glycolysis. *J. Biol. Chem.* **296**, 100736 (2021).
29. Hanna, D. A., Vitvitsky, V. & Banerjee, R. A growth chamber for chronic exposure of mammalian cells to H₂S. *Anal. Biochem.* **673**, 115191 (2023).
30. Carballal, S. et al. Hydrogen sulfide stimulates lipid biogenesis from glutamine that is dependent on the mitochondrial NAD(P)H pool. *J. Biol. Chem.* **297**, 100950 (2021).
31. De Bock, K. et al. Role of PFKFB3-driven glycolysis in vessel sprouting. *Cell* **154**, 651–663 (2013).
32. Diebold, L. P. et al. Mitochondrial complex III is necessary for endothelial cell proliferation during angiogenesis. *Nat. Metab.* **1**, 158–171 (2019).
33. Kumar, R. et al. A redox cycle with complex II prioritizes sulfide quinone oxidoreductase-dependent H₂S oxidation. *J. Biol. Chem.* **298**, 101435 (2022).
34. Spinelli, J. B. et al. Fumarate is a terminal electron acceptor in the mammalian electron transport chain. *Science* **374**, 1227–1237 (2021).
35. Marutani, E. et al. Sulfide catabolism ameliorates hypoxic brain injury. *Nat. Commun.* **12**, 3108 (2021).
36. Jackson, M. R. et al. Discovery of a first-in-class inhibitor of sulfide:quinone oxidoreductase that protects against adverse cardiac remodeling and heart failure. *Cardiovasc. Res.* **118**, 1771–1784 (2022).
37. Mansfield, K. D., Simon, M. C. & Keith, B. Hypoxic reduction in cellular glutathione levels requires mitochondrial reactive oxygen species. *J. Appl. Physiol.* **97**, 1358–1366 (2004).
38. Singhal, R. et al. HIF-2α activation potentiates oxidative cell death in colorectal cancers by increasing cellular iron. *J. Clin. Invest.* **131**, e143691 (2021).
39. Maclean, K. N. et al. Cystathionine β-synthase is coordinately regulated with proliferation through a redox-sensitive mechanism in cultured human cells and *Saccharomyces cerevisiae*. *J. Cell. Physiol.* **192**, 81–92 (2002).
40. Shi, Y. et al. Chronic hypoxia increases endothelial nitric oxide synthase generation of nitric oxide by increasing heat shock protein 90 association and serine phosphorylation. *Circ. Res.* **91**, 300–306 (2002).
41. Hampl, V., Cornfield, D. N., Cowan, N. J. & Archer, S. L. Hypoxia potentiates nitric oxide synthesis and transiently increases cytosolic calcium levels in pulmonary artery endothelial cells. *Eur. Respir. J.* **8**, 515–522 (1995).
42. Justice, J. M., Tanner, M. A. & Myers, P. R. Endothelial cell regulation of nitric oxide production during hypoxia in coronary microvessels and epicardial arteries. *J. Cell. Physiol.* **182**, 359–365 (2000).
43. Min, J. et al. Hypoxia-induced endothelial NO synthase gene transcriptional activation is mediated through the tax-responsive element in endothelial cells. *Hypertension* **47**, 1189–1196 (2006).
44. Ida, T. et al. Reactive cysteine persulfides and S-polythiolation regulate oxidative stress and redox signaling. *Proc. Natl Acad. Sci. USA* **111**, 7606–7611 (2014).
45. Yadav, P. K. et al. Biosynthesis and reactivity of cysteine persulfides in signaling. *J. Am. Chem. Soc.* **138**, 289–299 (2016).
46. Wedmann, R. et al. Improved tag-switch method reveals that thioredoxin acts as depersulfidase and controls the intracellular levels of protein persulfidation. *Chem. Sci.* **7**, 3414–3426 (2016).

47. Wang, W. Y., Lin, D., Jarman, E. H., Polacheck, W. J. & Baker, B. M. Functional angiogenesis requires microenvironmental cues balancing endothelial cell migration and proliferation. *Lab Chip* **20**, 1153–1166 (2020).
48. Titov, D. V. et al. Complementation of mitochondrial electron transport chain by manipulation of the NAD⁺/NADH ratio. *Science* **352**, 231–235 (2016).
49. Cherepanova, O. A. & Byzova, T. V. Pentose phosphate pathway drives vascular maturation. *Nat. Metab.* **4**, 15–16 (2022).
50. Vizan, P. et al. Characterization of the metabolic changes underlying growth factor angiogenic activation: identification of new potential therapeutic targets. *Carcinogenesis* **30**, 946–952 (2009).
51. Pugh, C. W. & Ratcliffe, P. J. Regulation of angiogenesis by hypoxia: role of the HIF system. *Nat. Med.* **9**, 677–684 (2003).
52. Li, X., Sun, X. & Carmeliet, P. Hallmarks of endothelial cell metabolism in health and disease. *Cell Metab.* **30**, 414–433 (2019).
53. Kabil, O. & Banerjee, R. Characterization of patient mutations in human persulfide dioxygenase (ETHE1) involved in H₂S catabolism. *J. Biol. Chem.* **287**, 44561–44567 (2012).
54. Libiad, M., Yadav, P. K., Vitvitsky, V., Martinov, M. & Banerjee, R. Organization of the human mitochondrial hydrogen sulfide oxidation pathway. *J. Biol. Chem.* **289**, 30901–30910 (2014).
55. Massari, S., Bosel, A. & Wrigglesworth, J. M. The variation of K_m for oxygen of cytochrome oxidase with turnover under de-energized and energized conditions. *Biochem. Soc. Trans.* **24**, 464S (1996).
56. Ast, T. & Mootha, V. K. Oxygen and mammalian cell culture: are we repeating the experiment of Dr. Ox? *Nat. Metab.* **1**, 858–860 (2019).
57. Petersen, L. C. The effect of inhibitors on the oxygen kinetics of cytochrome c oxidase. *Biochim. Biophys. Acta* **460**, 299–307 (1977).
58. Intlekofer, A. M. et al. Hypoxia induces production of L-2-hydroxyglutarate. *Cell Metab.* **22**, 304–311 (2015).
59. Oldham, W. M., Clish, C. B., Yang, Y. & Loscalzo, J. Hypoxia-mediated increases in L-2-hydroxyglutarate coordinate the metabolic response to reductive stress. *Cell Metab.* **22**, 291–303 (2015).
60. Berger, R. S. et al. Lactonization of the oncometabolite D-2-hydroxyglutarate produces a novel endogenous metabolite. *Cancers* **13**, 1756 (2021).
61. Pan, X. et al. A genetically encoded tool to increase cellular NADH/NAD⁺ ratio in living cells. *Nat. Chem. Biol.* <https://doi.org/10.1038/s41589-023-01460-w> (2023).
62. Ji, M. et al. Methionine restriction-induced sulfur deficiency impairs antitumour immunity partially through gut microbiota. *Nat. Metab.* **5**, 1526–1543 (2023).
63. Hine, C. et al. Endogenous hydrogen sulfide production is essential for dietary restriction benefits. *Cell* **160**, 132–144 (2015).
64. Jia, J. et al. SQR mediates therapeutic effects of H₂S by targeting mitochondrial electron transport to induce mitochondrial uncoupling. *Sci. Adv.* **6**, eaaz5752 (2020).

Publisher's note Springer Nature remains neutral with regard to jurisdictional claims in published maps and institutional affiliations.

Springer Nature or its licensor (e.g. a society or other partner) holds exclusive rights to this article under a publishing agreement with the author(s) or other rightsholder(s); author self-archiving of the accepted manuscript version of this article is solely governed by the terms of such publishing agreement and applicable law.

© The Author(s), under exclusive licence to Springer Nature America, Inc. 2024

Methods

Materials

Sodium sulfide nonahydrate (431648), sodium sulfite (S0505), sodium thiosulfate (217263), L-glutathione reduced (G4251), L-glutathione oxidized (G4501), L-cystine dihydrochloride (C6727), L-cysteine hydrochloride (C6852), L-arginine monohydrochloride (A5131), doxycycline (D3447), puromycin (P8833), protease inhibitor cocktail for mammalian tissue extract (P8340), RIPA lysis buffer (R0278), cystathionine (C3633), D-glucose (G7021), dimethyl sulfoxide (D2650), uridine (U3003), hydrocortisone (H0888) and glybenclamide (G0639) were from Sigma. RPMI-1640 (11875-093), Dulbecco's modified Eagle medium (DMEM; 11995-065), fetal bovine serum (FBS; 10437-028), trypsin-EDTA (25300-054), penicillin–streptomycin (15140-122), geneticin (10131-035), epidermal growth factor (EGF; PHG0311), PBS (10010-023), DPBS (14040-133), MCDB 131 (10372-019), sodium pyruvate (11360-070), trypan blue (15250-061) and ACK lysis buffer (A1049201) were from Gibco. Vascular cell basal medium (PCS 100-030), DPBS (30-2200), an endothelial cell growth kit (PCS 100-041), trypsin-EDTA (PCS 999-03) and trypsin neutralizing solution (PCS 999-04) were from ATCC. Dispase was from STEMCELL Technologies (07913). Carboxy PTIO (81540), DETA NONOate (82120) and FG4592 were from Cayman Chemical. L-[³⁵S]Methionine (NEG009A500UC) was from PerkinElmer. Collagenase type I (LS004196) was from Worthington Biochemical, and DNase I (1 U μ l⁻¹; 89836) was from Thermo Scientific. eNOS (1:1,000; 9572S, Cell Signaling Technology), Ki67 (1:400; 12202T, Cell Signaling Technology), HIF-1 α (1:1,000; ab179483, Abcam), HIF-2 α (1:1,000; A700-003, Bethyl Lab), CD31 (1:500; 28083-1AP, Proteintech), CD31-PE (1:100; 12-0311-82, eBiosciences), CD45-APC-eFluor 780 (1:100; 47-0451-82, eBiosciences), SQOR (1:2,000; 17256-1AP, Proteintech) and Flag (1:2,000; F1804, Sigma) antibodies and the secondary anti-rabbit horseradish peroxidase-linked IgG antibody (1:10,000; NA944V, GE Healthcare (for western blotting) and 7074S, Cell Signaling Technology (for IHC)) were purchased from the indicated vendors. DyLight 649-labeled UEA (1:200, Vector Labs), EdU (ClickIT EdU, Life Technologies), tamoxifen (10540-29-1, MCE), formalin (Fisher Scientific, SF98-4), SG-209 (T24786, TargetMol), EZ prep solution (950-102), DISCOVERY Cell Conditioning 1 Buffer (950-500), Reaction Buffer Concentrate (950300), omniMap anti-rabbit horseradish peroxidase (760-4311), ChromoMap DAB (760-159) from Ventana Medical Systems (Roche Diagnostics), hematoxylin stain, Gill II (Newcomer Supply), NAD/NADH-Glo kit (G9071, Promega), Quick RNA Microprep kit (R1050, Zymo Research), SuperScript III One-Step RT-PCR System with Platinum Taq DNA Polymerase (12574026, Invitrogen) and SYBR Green PCR master mix (4309155, Applied Biosystems) were from the indicated vendors.

Cell culture

EA.hy926 and HEK293 cells were cultured in DMEM. HMEC-1 cells were cultured in MCDB 131 with 10 ng ml⁻¹ EGF, 1 μ g ml⁻¹ hydrocortisone and 10 mM glutamine. HUVECs were cultured in vascular cell basal medium, to which the endothelial cell growth kit was added to obtain final concentrations of the following growth factors: VEGF (5 ng ml⁻¹), recombinant human (rh) EGF (5 ng ml⁻¹), rhFGF basic (5 ng ml⁻¹), rhIGF-1 (5 ng ml⁻¹), L-glutamine (10 mM), heparin sulfate (0.75 U ml⁻¹), hydrocortisone hemisuccinate (1 μ g ml⁻¹) and ascorbic acid (50 μ g ml⁻¹). The following cell lines were cultured in the specified media: HepG2 cells (Eagle minimum essential medium containing 2 mM glutamine), 143B cells (DMEM supplemented with 100 μ g ml⁻¹ uridine) and SH-SY5Y cells (DMEM/F12). All culture media were supplemented with 1% penicillin–streptomycin and 10% FBS except the medium for HUVECs, which contained 2% FBS. Cells were cultured in 5% CO₂ incubators with humidified ambient air containing 21% O₂ (normoxia chamber) or with 93% N₂, 5% CO₂ and 2% O₂ (hypoxia chamber).

Animal studies

All experiments were performed with approval from the Institutional Animal Care and Use Committee at the University of Michigan. Animals were maintained under standard housing conditions (temperature of 22 \pm 2 °C and humidity ranging from 30% to 70%) with ad libitum access to food and water and a 12-h light/12-h day cycle.

Generation of *Sqor*^{fl/fl}-knockout mice

Sqor^{loxP/+} mice were generated by Cyagen Biosciences. Briefly, the targeting vector was constructed by inserting one self-deletion anchor-flanked neomycin cassette and two *loxP* sites flanking exon 7 of *Sqor* and electroporating into embryonic stem cells from C57BL/6N mice. The transfected embryonic stem cells were subjected to G418 selection (200 μ g ml⁻¹) 24 h after electroporation. G418-resistant clones were picked and amplified in 96-well plates. The following primers were used for screening targeted clones: 5'-AGTTTCAAGGCTCTAACATCTCCT-3' (forward) and 5'-AATACCTTCAATAGGAGAGATGGGG-3' (reverse). The positive clones were expanded and further characterized by Southern blotting, injected into C57BL/6N embryos and reimplanted in CD1 pseudopregnant females. Following a subsequent cross with C57BL/6N animals, the *neo* transgene was removed, and the *Sqor*^{loxP/+} mice were generated. The following primers used to identify *neo* deletion: 5'-TTTTCTTCTGCCTAAAACCCTGC-3' (forward 1) and 5'-AATCTAAAAGGCAATTCTCCCCATC-3' (reverse 1). An inducible whole-body disruption of *Sqor* was generated by crossing *Sqor*^{loxP/loxP} mice with CAGG-Cre^{ER} mice (The Jackson Laboratory, 004682). An inducible endothelial-specific disruption of *Sqor* was generated by crossing *Sqor*^{loxP/loxP} mice with VE-cadherin-Cre^{ERT2} mice⁶⁵.

[³⁵S]Methionine flux into glutathione

Cells were seeded in 6-cm plates at a density of 2.4 million cells per plate, except HUVECs (1.2 million cells per plate), and were allowed to settle overnight (15–18 h). The cells were washed twice with 2 ml of 1 \times PBS (pH 7.4) before 4 ml of fresh medium was added, except for HUVEC cultures in which 2 ml of medium per 6-cm plate was added. Each culture medium also contained either 5 μ Ci ml⁻¹ [³⁵S]methionine (EA.hy926, HMEC-1 and HUVECs) or 2.5 μ Ci ml⁻¹ [³⁵S]methionine, and cells were incubated for 24 h under normoxic (21% O₂) or hypoxic (2% O₂) conditions except for HUVECs, which were incubated for 16 h. The medium was then aspirated, and the cells were washed twice with 1 \times PBS and scraped in 150 μ l of 1 \times PBS to obtain cell suspensions. For the analysis of radiolabel incorporation in GSH, 100 μ l of each cell suspension was mixed with an equal volume of metaphosphoric acid solution (135 mM metaphosphoric acid, 5 mM EDTA and 150 mM NaCl), vortexed and stored at -20 °C. For protein quantitation, 30 μ l of cell suspension was mixed with an equal volume of RIPA buffer with protease inhibitor and stored at -20 °C. The protein concentration in the cell suspension was measured using Bradford reagent (Bio-Rad).

To measure radiolabel incorporation into GSH, cell samples were treated and analyzed by HPLC, as described previously^{66,67}. Briefly, samples were thawed, vortexed and centrifuged at 12,000g for 5 min at 4 °C. The supernatant (150 μ l) was mixed with 15 μ l of iodoacetic acid (14 mg ml⁻¹) to alkylate thiols, the pH was adjusted to 7–8 with saturated potassium carbonate using pH paper, and the mixture was incubated for 1 h at room temperature in the dark. An equal volume of 2,3-dinitrofluorobenzene (1.5% (vol/vol) in absolute ethanol) was then added to derivatize amino groups and incubated at room temperature for 4 h in the dark. Cystine, cysteine and GSH were separated by HPLC using a Bondapak NH₂ column (300 mm \times 3.9 mm, 10 μ m; Waters) at a flow rate of 1 ml min⁻¹. The mobile phase consisted of solution A (80% methanol in water) and solution B, which was prepared by mixing 154.9 g of ammonium acetate in 100 ml of water and 400 ml of glacial acetic acid and adding 150 ml of the resulting solution to 300 ml of solvent A. The mobile phase comprised 0 to 10 min isocratic 25% solution B and 10 to 30 min linear gradient from 25 to 100% solvent B.

The elution of metabolites was monitored by absorbance at 355 nm. The column was equilibrated with 30% solvent B before samples (50–100 μ l) were injected. The concentration of metabolites (cystine, cysteine and GSH) was determined by comparing the integrated peak area with a calibration curve generated for each compound. Incorporation of [35 S]methionine into GSH was determined by measuring radioactivity in the corresponding chromatographic fraction, and the data were normalized to protein concentration.

Extracellular thiosulfate and intracellular glutathione, glutathione disulfide and cysteine quantitation

Cells were seeded similar to as described above, and the following day, cells were washed twice with 2 ml of 1 \times PBS, switched to fresh medium (3 ml) and cultured at 2% or 21% O₂. Extracellular thiosulfate was determined in the conditioned medium at 24 h (and in some cases at 4 h). The medium from HUVECs cultured in DMEM was collected at 16 h. Thiosulfate levels were quantified in each culture medium to obtain blank values. For thiosulfate derivatization, 45 μ l of culture medium was mixed with 2.5 μ l of Tris base (1 M) and 2.5 μ l monobromobimane (60 mM). The mixture was vortexed and incubated at room temperature in the dark for 10 min. Proteins in the derivatized mixture were then precipitated using metaphosphoric acid (16.8 mg ml⁻¹). Samples were centrifuged at 12,000g for 5 min at 4 °C, and the supernatant was collected in the dark and stored at -20 °C until further use.

A Zorbax Eclipse XDB-C18 column (5 μ m, 4.6 \times 150 mm; Agilent) was used to separate thiosulfate using an ammonium acetate/methanol buffer system with the following gradient: solution A contained 100 mM ammonium acetate (pH 4.75) and 10% methanol; solution B contained 100 mM ammonium acetate (pH 4.75) and 90% methanol. The percentage of B was increased in the gradient as follows: 0–10 min, linear 0 to 20%; 10–15 min, linear 20 to 50%; 15–20 min, isocratic 50%; 20–22 min, 50 to 100%; 22–27 min, isocratic 100%; 27–29 min, linear 100 to 0%; 29–35 min, isocratic 0%. Thiosulfate was detected using excitation and emission wavelengths set at 390 nm and 490 nm, respectively. The column was calibrated with known concentrations of derivatized sodium sulfide, sodium sulfite and sodium thiosulfate.

For GSH and GSSG quantitation, scrambled, *SQOR*-KD and *ETHE1*-KD EA.hy926 cells were seeded in 6-cm plates at a density of 2 million–2.5 million cells per plate and were allowed to settle overnight (15–18 h). Fresh medium was added, and cells were cultured in either 2% or 21% O₂ for 24 h. Cell collection, sample preparation, protein quantitation and HPLC analysis of GSH and GSSG were performed as described in [35S]Methionine flux into glutathione.

Cysteine was quantified in cystathionine-treated EA.hy926 cells that were seeded in 6-cm plates at a density of 2 million cells per plate and were allowed to settle overnight (15–18 h). Fresh medium was then added, and cells were treated with 100 μ M cystathionine (dissolved in 50 mM NaOH) or an equal volume of the vehicle for 24 h. Sample preparation and cysteine analysis were performed as described in [35S]Methionine flux into glutathione.

Cellular hydrogen sulfide consumption assay

EA.hy926 cells were grown to ~90% confluency in 10-cm plates, washed with PBS and treated with 0.05% trypsin-EDTA (for ~6–8 min at 37 °C). Cells were then resuspended in 10 ml of complete medium (DMEM + 10% FBS + 1% penicillin–streptomycin) and centrifuged for 5 min at 4 °C and 1,700g. The cell pellet was resuspended in 1 ml of modified DPBS (supplemented with 20 mM HEPES (pH 7.4) and 5 mM glucose) in a preweighed Eppendorf tube and centrifuged for 5 min at 4 °C and 1,700g. The supernatant was discarded, and the pellet weight was determined. Cells were suspended in modified DPBS to make a 10% cell suspension (wt/vol) in a 1-ml Eppendorf tube. Cells were then treated with 100 μ M Na₂S. The suspension cultures were incubated at 37 °C with shaking (75 rpm). Na₂S (100 μ M) in modified DPBS was incubated in parallel, and the concentration of H₂S lost from

these samples was subtracted from the values obtained from the cell suspension samples containing the same reagents. Following monobromobimane derivatization, HPLC was used to quantitate H₂S levels as described above.

Short hairpin RNA knockdowns and *L. brevis* NADH oxidase expression

The pLKO.1 vector containing shRNAs was purchased from Sigma. The following clone IDs were used: *SQOR* (TRCN0000039004 and TRCN0000039006), *ETHE1* (TRCN0000083454 and TRCN0000083455) and *NOS3* (TRCN0000045476, TRCN0000045477 and TRCN0000414816). pZIP-HIF-1 and pZIP-HIF-2-alpha were from the Shah lab (Department of Molecular and Integrative Physiology, University of Michigan), and the pINDUCER empty vector or vector containing mitochondrial *LbNOX* was from the Lysiotis lab (University of Michigan). shRNA (2.5 μ g) containing plasmids was submitted to the University of Michigan Vector Core for lentiviral packaging. To generate shRNA-induced KDs, cells were seeded at a density of 7.5 \times 10⁴ cells in a six-well plate containing 2 ml of culture medium per well. The next day, the medium was changed, and cells were transduced with the optimized viral titer for 48 h in the presence of polybrene (8 μ g ml⁻¹). The medium was then replaced with virus-free medium, and growth was continued for an additional 24 h. Puromycin (1 μ g ml⁻¹) was used to select KD cells, whereas geneticin (500 μ g ml⁻¹) was used for the selection of mito-*LbNOX*-expressing cells. A combination of puromycin (1 μ g ml⁻¹) and geneticin (500 μ g ml⁻¹) was used for *LbNOX* expression in the *SQOR*-KD background. Once the cells were confluent, they were transferred to 10-cm plates. Selection was continued for ~2 weeks, and KD efficiency and *LbNOX* expression were estimated by western blotting.

Western blotting

Three 10-cm plates with confluent EA.hy926 cells were washed twice with 1 \times PBS, scraped in 750 μ l of 1 \times PBS and pooled. After centrifugation at 1,700g for 5 min at 4 °C, the supernatant was discarded, and the pellet was dissolved in 100 μ l of RIPA buffer containing protease inhibitor and vortexed. Three freeze–thaw cycles and vortexing yielded efficient cell lysis, and the supernatant was collected after centrifugation at 12,000g for 5 min at 4 °C. The supernatant obtained after cell lysis was used to determine the protein concentration using a Bradford assay. The supernatant was then mixed with 4 \times sample buffer to obtain a final concentration of 2 μ g of protein per μ l, heated at 95 °C for 5 min and used immediately for western blotting or stored at -80 °C for up to 2 weeks. Protein was separated on a 10–12% SDS polyacrylamide gel and transferred to a PVDF membrane. Membranes were incubated overnight at 4 °C with primary antibodies with the following dilutions: *SQOR* (1:2,000), *ETHE1* (1:1,000), eNOS (1:2,000), HIF-1 (1:1,000), HIF-2 (1:1,000) and anti-Flag (1:2,000). The secondary antibody, horseradish peroxidase-linked anti-rabbit IgG, was used at a 1:10,000 dilution. Blots were developed with KwikQuant Digital-ECL substrate (KwikQuant), and images were collected with a KwikQuant Imager. Equal loading was verified by Ponceau S staining of membranes or with anti-actin for HIF-1 and HIF-2.

Proliferation assay

Cells were seeded at a density of 10,000–50,000 in 2 ml of medium and grown overnight in six-well plates under standard cell culture conditions (37 °C, 5% CO₂ and ambient air). The medium was changed (2 ml) the next day, and cells were placed in 21% or 2% O₂ incubators. Cells were counted starting 24 h later and every 24 h for 4 days. For this, cells were washed twice with 2 ml of 1 \times PBS, and 500 μ l of 0.05% trypsin (0.25% for HMEC-1 cells) was added and placed at 37 °C for 5–7 min. The cells were then resuspended with 500 μ l of medium and centrifuged at 4 °C for 5 min. The supernatant was discarded, the cell pellet was resuspended in 50 μ l of medium (as specified for each cell line above) and diluted

1:1 (vol/vol) with trypan blue, and 20 μ l of the resulting sample was counted using a Cellometer (Nexcelcom).

Clonogenic assay

Cells were seeded in a six-well plate at a density of 500 cells per well with each well containing 2 ml of culture medium and grown overnight under standard cell culture conditions (37 °C, 5% CO₂ and 21% O₂). The next day, cells were placed in 2% or 21% O₂ incubators and grown for 10–12 days with fresh medium changes every 3–4 day. Culture medium used for cells growing in 2% O₂ was placed in the hypoxic chamber overnight before use. Once colonies were visible, the medium was aspirated, and cells were washed twice with 1 \times PBS, fixed with 10% buffered formalin for 20 min and incubated in crystal violet solution (0.5% crystal violet in 20% methanol) for 35 min. The wells were then washed six times with 4 ml of distilled water to remove residual stain, dried in an inverted position overnight and imaged. Colonies were counted for quantitation, and any colony containing less than 5 pixels was excluded from the analysis.

Tube formation assay

Corning Matrigel was thawed on ice, and 200–250 μ l was added per well in a 24-well plate using chilled tips and placed in a 37 °C incubator for 30 min to coat the wells. In total, 1.2 \times 10⁵ EA.hy926 and HMEC-1 (scrambled and *SQOR*-KD) cells were seeded in DMEM (160 μ l) with 10% FBS and 1% penicillin–streptomycin and diluted 1:1 with incomplete DMEM (without FBS; 160 μ l) to obtain a final FBS concentration of 5%. The cells were then placed in a 21% O₂ incubator for 1 h before being switched to the 2% O₂ incubator. Cells were imaged with a BioTek BioSpa Live Cell Analysis System after 18 h. ImageJ with the angiogenesis plugin was used to quantify the angiogenic parameters specified in the figure legend⁶⁸.

Sprouting assay in a microfluidic device

Microfluidic devices were prepared as previously described⁴⁷. Briefly, polydimethylsiloxane was cast into previously established three-dimensional printed molds and bonded to glass coverslips with a plasma etcher. Devices were treated with 0.01% (wt/vol) poly-L-lysine and 0.5% (wt/vol) L-glutaraldehyde sequentially to promote extracellular matrix attachment to the polydimethylsiloxane housing. Stainless steel acupuncture needles (300 μ m; Lhasa OMS) were threaded into each device, and type I rat tail collagen (Corning) was prepared similar to as described in Doyle⁶⁹ and polymerized around each needle for 30 min at 37 °C. Collagen gels were hydrated overnight. DMEM and needles were removed to form three-dimensional hollow channels embedded within the collagen. A 10- μ l suspension of cells (2 million cells per ml) was added to one reservoir of the endothelial channel and inverted for 30 min to allow cell attachment, followed by a second seeding with the device upright. Devices were cultured with continual reciprocating flow using gravity-driven flow on a seesaw rocker plate at 0.33 Hz. VEGF (Peprotech) was supplemented in culture medium at 10 ng ml⁻¹ for 48 h, and the medium was refreshed every 24 h. Culture medium was further supplemented with EdU for the final 24 h. Tip cell formation was quantified via a custom MATLAB image analysis code with tip cells denoted as any nuclei fully outside of the cell channel edge. Cultures were fixed in 4% paraformaldehyde and permeabilized with a PBS solution containing Triton X-100 (5% vol/vol), sucrose (10% wt/vol) and magnesium chloride (0.6% wt/vol) for 1 h each at room temperature. DAPI (1 μ g ml⁻¹) was used to visualize cell nuclei. For proliferation studies, EdU fluorescent labeling was performed following the manufacturer's protocol (ClickIT EdU, Life Technologies). DyLight 649-labeled UEA (1:200, Vector Labs) was used to visualize endothelial cell location. Fluorescent images were captured on a Zeiss LSM800 confocal microscope.

Glucose and lactate quantitation

Glucose and lactate quantitation was performed in the culture medium as previously described²⁸. Briefly, 100 μ l of medium was removed and mixed with 200 μ l of 5% HClO₄, vortexed and stored at -20 °C until use.

On the day of analysis, samples were thawed on ice, vortexed and centrifuged at 13,000g for 5 min at 4 °C. The supernatant was collected and neutralized to pH 7 with saturated K₂CO₃ solution. The concentrations of glucose and lactate in the neutralized supernatants were measured using a D-GLUCOSE-HK kit (Megazyme) and an L-Lactate Assay kit (Cayman Chemical), as per the manufacturers' protocols.

Tumor angiogenesis assay

Sqor^{fl/fl}, WB^{Cre}*Sqor*^{fl/fl} and VE-cadherin^{Cre-ERT2}*Sqor*^{fl/fl} (both sexes) were administered five doses of 10 mg per kg (body weight) tamoxifen (10 mg ml⁻¹ in corn oil) at 48-h intervals. The lower flanks of the mice were then implanted with 2 \times 10⁶ (experiment 1, with *Sqor*^{fl/fl} versus WB^{Cre}*Sqor*^{fl/fl} mice) or 2.5 \times 10⁵ (experiment 2, with *Sqor*^{fl/fl} versus WB^{Cre}*Sqor*^{fl/fl} and *Sqor*^{fl/fl} versus VE-cadherin^{Cre-ERT2}*Sqor*^{fl/fl} mice) YUM5.2 cells in 100 μ l of 1 \times PBS. In experiment 2, tumor size was measured using calipers every 2–3 days for 23 days, and tumor volume was calculated by first determining the geometric mean between the length and width and then using the following equation^{32,70}:

$$\left[\frac{4}{3} \times \pi \times (\text{geometric mean}/2)^3 \right]$$

Mice were killed, tumors were excised, and the tumors were weighed. Tumor cross-sections were prepared for histological and immunohistochemical analyses.

Immunohistochemistry

Histology was performed at the University of Michigan Center for Gastrointestinal Research. Tumor tissue and gastrocnemius muscle were fixed in formalin for 24 h and embedded in paraffin. Sectioning (5- μ m thickness) was performed using a microtome (Leica, RM 2125 RT). The Discovery Ultra (autostainer) platform was used for immunohistochemistry, which involves the following steps. Deparaffinization of tumor and muscle sections was performed for 24 min at 69 °C in EZ prep solution. Next, antigen retrieval was performed in cell conditioning 1 buffer at 95 °C for 40 min. Blocking was performed by inhibitor ChromoMap for decreasing endogenous peroxidase activity at 37 °C for 8 min. Sections were stained with anti-K67 (1:250) and anti-CD31 (1:200) for 60 min at 40 °C and washed with reaction buffer (Tris-based buffer with preservatives, pH 7.4–7.8; Ventana Medical). Sections were treated with OmniMap anti-rabbit horseradish peroxidase, incubated for 28 min and treated with ChromoMap DAB solution for 5 min. Sections were counterstained by hand with five quick dips in Gill II hematoxylin stain, and residual stain was removed with the wash buffer. Sections were dehydrated in 95% alcohol for 5 min before mounting with Permونت mounting medium. Slides were scanned using a Panoramic scanner and analyzed using CaseViewer version 1.4 (Caliper Life Sciences). Images were imported into ImageJ and deconvoluted using color deconvolution 2 into the hematoxylin and Ki67 or CD31 channels. The same threshold was applied to all images to quantify Ki67 and CD31 intensity, and values were normalized to the image area and are expressed as a percentage of control.

Metabolomics sample preparation

EA.hy926, HMEC-1 and HUVECs were seeded at a density of 1 million cells per well. The next day, the medium was aspirated and replaced with fresh medium, and the cells were cultured in a normoxic or hypoxic incubator for 24 h. For intracellular metabolites, the medium was aspirated, and cells were scraped with 1 ml of ice-cold 80% methanol, collected in 1.5-ml Eppendorf tubes and incubated on dry ice for 10 min. The samples were then centrifuged at 12,000g. The supernatant was collected and dried using a SpeedVac concentrator. The sample was dissolved in 50% (vol/vol) methanol in water and analyzed by liquid chromatography–mass spectrometry using Agilent MassHunter Workstation software for 6400 Series Triple Quadrupole MS with version B.08.02, as described in detail previously⁷¹.

Hind limb ischemia through femoral artery ligation

Sqor^{fl/fl} and *WB^{Cre}Sqor^{fl/fl}* mice were administered tamoxifen (10 mg ml⁻¹ in corn oil) via daily intraperitoneal injection (100 mg per kg (body weight)) for five consecutive days. Surgery was performed at the Physiology Phenotyping Core (University of Michigan). Briefly, *Sqor^{fl/fl}* and *WB^{Cre}Sqor^{fl/fl}* mice were anesthetized with isoflurane, and a circulating heated waterpad was used to maintain body temperature. An ~1-cm-long incision was made from the knee toward the medial left thigh. Subcutaneous fat tissue surrounding the thigh muscle was gently brushed away using sterile saline-moistened fine-pointed cotton swabs to reveal the underlying femoral artery. Fine forceps and a fine-pointed cotton swab was used to gently pierce through the membranous femoral sheath to expose the neurovascular bundle. Silk sutures were used to double ligate the femoral artery proximal to the superficial caudal epigastric artery and transect between the two ligatures. The incision was closed using stainless steel wound clips⁷².

Laser doppler imaging

Laser doppler imaging was performed at the Physiology Phenotyping Core (University of Michigan) following Institutional Animal Care and Use Committee guidelines. Briefly, the body temperature of anesthetized mice was monitored with a rectal probe, and respiration patterns and tail and ear color were monitored for cardiovascular function. Mice were anesthetized individually with an isoflurane precision vaporizer anesthetic machine by first placing them in an induction chamber and introducing isoflurane along with approximately 1 l of oxygen until the animal was recumbent and breathing had slowed. The animal was then removed from the induction chamber and placed on a circulating heating pad designed for rodent surgery and temperature regulation and was subjected to presurgery anesthesia testing by toe pinch. Fur was either shaved using animal clippers and/or completely removed with depilatory cream. Noninvasive imaging was performed with a Perimed Laser Doppler scanning system with a surface probe over a period of 30 min. Because the scanner does not contact the animal, medium is not applied to the surface. Imaging was performed on the ventral surface of the hind limbs on days 1, 3 and 8 after surgery.

Spheroid culture

Cells were detached with 0.25% trypsin-EDTA and counted, and ~200 cell-sized spheroids were grown overnight in inverse pyramidal polydimethylsiloxane microwells (AggreWell, STEMCELL Technologies) treated with 0.5% Pluronic F-127 to prevent cell adhesion. Spheroids were collected and centrifuged to remove residual single cells. The spheroids (~6,000 spheroids per ml) were encapsulated in 3 mg ml⁻¹ type I rat tail collagen (Corning). VEGF (100 ng ml⁻¹, Peprotech) and EdU (10 μM) were added to the culture medium to promote tip cell formation and enable visualization of proliferation, respectively. After 48 h, spheroids were fixed in 4% paraformaldehyde and permeabilized with a PBS solution containing Triton X-100 (5% vol/vol), sucrose (10% wt/vol) and MgCl₂ (0.6% wt/vol) for 1 h at room temperature. DAPI (1 μg ml⁻¹) was used to visualize cell nuclei. For proliferation studies, fluorescent EdU labeling was performed following the manufacturer's protocol (ClickIT EdU, Life Technologies). DyLight 649-labeled UEA (1:200, Vector Labs) was used to visualize endothelial cells. Fluorescent images were recorded using a Zeiss LSM800 confocal microscope.

Lung endothelial cell isolation by fluorescence-activated cell sorting

Lungs were collected from four mice from each of the two groups, *Sqor^{fl/fl}* and *VE-cadherin^{Cre-ERT2}Sqor^{fl/fl}*. First, mice were transcardially perfused for 5 min at 2 ml min⁻¹ with ice-cold PBS and then with dispase solution (0.25 U ml⁻¹). Lungs were collected, cut into small pieces and digested while shaking in dissociation solution (PBS) containing collagenase type I (5 mg ml⁻¹) and DNase I (1 mg ml⁻¹) at 37 °C for 45 min. The sample was then homogenized by passing through a 28-gauge needle multiple

times and then through a 70-μm filter (Fisherbrand, Sterile Cell Strainer). Red blood cell lysis was performed with ACK lysis buffer (Gibco) for 5 min and stopped with PBS + 2% FBS (FACS buffer). Centrifugation was performed at 400g for 5 min, and the cell pellet was incubated with anti-mouse-CD45-APC (1:100) and anti-mouse-CD31-PE (1:100) for 45 min at 4 °C. After staining, cells were washed twice with FACS buffer and resuspended in 3 ml of PBS. A Sony SH800 Cell Sorter running on software version 2.1.0 using a two-way sorting system was used. Cells were gated using forward scatter (FSC) and back scatter (BSC). Doublets were excluded by using both FSC width versus FSC area and BSC width versus BSC area. Two populations were sorted by gating CD31-PE⁺CD45-APC⁺ (leukocytes) and CD31-PE⁺CD45-APC⁻ (endothelial cells). A sorting efficiency of >80% was maintained throughout the procedure. In total, 2 million leukocytes and 1 million endothelial cells were sorted from each sample. The purity (80–90%) of the sorted fraction was assessed by FACS.

Real-time quantitative PCR

Total RNA was extracted from endothelial cells sorted by FACS using a Quick RNA microprep kit (Zymo Research), as per the manufacturer's instructions. RNA (500 ng) was reverse transcribed to cDNA using a SuperScript III First-Strand Synthesis System (Invitrogen). Real-time PCR reactions were set up in three technical replicates for each sample. The following primer pairs were used for amplification:

5'-GAGTTGGAGCAGAGAATGTGGC-3' and 5'-CACACTCAGTGTGGAACGGACT-3' (*SQOR*), 5'-GGAGTCAAGAGAGGCCAGTCTGTC-3' and 5'-GTGATGTGGTCAGCATGGCAGTC-3' (*ETHE1*) and 5'-GGCTGTATCCCTCCACG-3' and 5'-CCAGTTGGTAACAATGCCATGT-3' (*ACTB*).

The cDNA, gene-specific primers and SYBR Green master mix (Applied BioSystems) were combined and run in a QuantStudio 5 Real-Time PCR System (Applied BioSystems). Relative gene expression was calculated using the change in cycling threshold (ΔΔC_t) method with *ACTB* as the housekeeping gene.

NAD⁺/NADH quantitation

EA.hy926 cells (scrambled and *SQOR* KD) were plated in 12-well plates (5 × 10⁵ cells per well with 2 ml of medium) and cultured for 24 h at 37 °C under normoxic (5% CO₂ in humidified air) or hypoxic (2% O₂ and 5% CO₂ in humidified N₂) conditions. The [NAD⁺]:[NADH] ratio was measured using an NAD/NADH-Glo assay kit (Promega), according to the manufacturer's protocol. Briefly, the medium was aspirated, and 200 μl of lysis solution (1:1 (vol/vol) mixture of PBS and bicarbonate buffer (containing 100 mM sodium bicarbonate, 20 mM sodium carbonate, 10 mM nicotinamide, 0.05% Triton X-100 and 1% (wt/vol) dodecyl trimethylammonium bromide)) was added to each well. After agitation for 2 min, 10-μl aliquots were removed from each well and added to sample tubes containing 90 μl of lysis solution (for NADH analysis) or 90 μl of lysis solution plus 50 μl of 0.4 N HCl (for NAD⁺ analysis). The samples were mixed by vortexing, incubated for 15 min at 60 °C and cooled for 10 min at room temperature. Then, 50 μl of 0.5 M Tris was added to the samples for NAD⁺ analysis, and 100 μl of the 0.4 N HCl/0.5 M Tris mixture (1:1 vol/vol) was added to the samples for NADH analysis. Finally, 50 μl of NAD/NADH-Glo Detection Reagent was added per well of a white 96-well plate followed by 50 μl of sample or blank (1:1 (vol/vol) mixture of lysis solution and the HCl/Tris mixture). Luminescence was measured after a 30-min incubation at room temperature. The [NAD⁺]:[NADH] ratio was calculated as the ratio of the luminescence intensities from the respective samples.

Reporting summary

Further information on research design is available in the Nature Portfolio Reporting Summary linked to this article.

Data availability

All data generated and analyzed in this study are included in the main text and Supplementary Information file. Source data are provided with this paper.

Code availability

The code used to analyze tip cells in the microfluidic device is available for download at <https://github.com/hirakih/Sulfide-oxidation-promotes-hypoxic-angiogenesis-and-neovascularization-MATLAB-Code>.

References

65. Wang, Y. et al. Ephrin-B2 controls VEGF-induced angiogenesis and lymphangiogenesis. *Nature* **465**, 483–486 (2010).
66. Mosharov, E., Cranford, M. R. & Banerjee, R. The quantitatively important relationship between homocysteine metabolism and glutathione synthesis by the transsulfuration pathway and its regulation by redox changes. *Biochemistry* **39**, 13005–13011 (2000).
67. Vitvitsky, V., Thomas, M., Ghorpade, A., Gendelman, H. E. & Banerjee, R. A functional transsulfuration pathway in the brain links to glutathione homeostasis. *J. Biol. Chem.* **281**, 35785–35793 (2006).
68. Carpentier, G. et al. Angiogenesis analyzer for ImageJ—a comparative morphometric analysis of ‘endothelial tube formation assay’ and ‘fibrin bead assay’. *Sci. Rep.* **10**, 11568 (2020).
69. Doyle, A. D. Generation of 3D collagen gels with controlled diverse architectures. *Curr. Protoc. Cell Biol.* **72**, 10.20.1–10.20.16 (2016).
70. Solanki, S. et al. Dysregulated amino acid sensing drives colorectal cancer growth and metabolic reprogramming leading to chemoresistance. *Gastroenterology* **164**, 376–391 (2023).
71. Kerk, S. A. et al. Metabolic requirement for GOT2 in pancreatic cancer depends on environmental context. *eLife* **11**, e73245 (2022).
72. Brenes, R. A. et al. Toward a mouse model of hind limb ischemia to test therapeutic angiogenesis. *J. Vasc. Surg.* **56**, 1669–1679 (2012).

Acknowledgements

This work was supported, in part, by grants from the National Institutes of Health (GM130183 to R.B., R01CA248160 to C.A.L. and R01CA148828 and R01CA245546 to Y.M.S.), the American Heart Association (826245 to R.K. and 19POST34380588 to S.S.), the American Physiology Society and Crohn’s and Colitis Foundation (1003279 to R.S. and 623914 to S.S.) and the National Institute of Dental and Cranofacial Research (T32DE00705745 to H.L.H.) and by T32 GM 132046 (National Institutes of Health) support to S.A. We acknowledge A. Landry and W. Huang (University of Michigan) for

their technical help with generating the SQOR KD in EA.hy926 cells and with collecting mouse samples, respectively. We acknowledge S. Whitesall in the Physiology Phenotyping Core at the University of Michigan for hind limb ischemia surgery and laser doppler perfusion imaging. We thank M. Mattea at the University of Michigan Center for Gastrointestinal Research for histology studies.

Author contributions

R.K., Y.M.S. and R.B. conceptualized the study, and R.K. performed and analyzed the majority of the experiments, with assistance from V.V. ($[^{35}\text{S}]$ methionine flux, glucose consumption assays and NAD⁺:NADH estimation), A.S. (proliferation assays), R.S. (HIF-1/HIF-2 western blots, YUMM5.2 culture, lung endothelial cell isolation FACS and real-time quantitative PCR), S.S. (tumor xenograft (experiment 2) and immunohistochemistry), S.A. (GSH, GSSG, cysteine quantitation and HIF-1 stabilization in KD cells), H.L.H. and B.M.B. (tip sprouting assay), H.N.B. (tumor xenograft (experiment 1)) and A.A. and C.A.L. (metabolomics data generation and analysis). R.K. and R.B. drafted the manuscript, and all authors edited and approved the final version.

Competing interests

C.A.L. has received consulting fees from Astellas Pharmaceuticals, Odyssey Therapeutics and T-Knife Therapeutics and is an inventor on patents pertaining to Kras-regulated metabolic pathways, redox control pathways in pancreatic cancer and targeting the GOT1 pathway as a therapeutic approach (US Patent number 2015126580-A1, 5 July 2015; US Patent number 20190136238, 9 May 2019; International Patent number WO2013177426-A2, 23 April 2015). The remaining authors declare no competing interests.

Additional information

Supplementary information The online version contains supplementary material available at <https://doi.org/10.1038/s41589-024-01583-8>.

Correspondence and requests for materials should be addressed to Ruma Banerjee.

Peer review information *Nature Chemical Biology* thanks Christopher Hine, Peter Nagy and the other, anonymous, reviewer(s) for their contribution to the peer review of this work.

Reprints and permissions information is available at www.nature.com/reprints.

Reporting Summary

Nature Portfolio wishes to improve the reproducibility of the work that we publish. This form provides structure for consistency and transparency in reporting. For further information on Nature Portfolio policies, see our [Editorial Policies](#) and the [Editorial Policy Checklist](#).

Statistics

For all statistical analyses, confirm that the following items are present in the figure legend, table legend, main text, or Methods section.

- | n/a | Confirmed |
|-------------------------------------|--|
| <input type="checkbox"/> | <input checked="" type="checkbox"/> The exact sample size (n) for each experimental group/condition, given as a discrete number and unit of measurement |
| <input type="checkbox"/> | <input checked="" type="checkbox"/> A statement on whether measurements were taken from distinct samples or whether the same sample was measured repeatedly |
| <input type="checkbox"/> | <input checked="" type="checkbox"/> The statistical test(s) used AND whether they are one- or two-sided
<i>Only common tests should be described solely by name; describe more complex techniques in the Methods section.</i> |
| <input checked="" type="checkbox"/> | <input type="checkbox"/> A description of all covariates tested |
| <input checked="" type="checkbox"/> | <input type="checkbox"/> A description of any assumptions or corrections, such as tests of normality and adjustment for multiple comparisons |
| <input type="checkbox"/> | <input checked="" type="checkbox"/> A full description of the statistical parameters including central tendency (e.g. means) or other basic estimates (e.g. regression coefficient) AND variation (e.g. standard deviation) or associated estimates of uncertainty (e.g. confidence intervals) |
| <input type="checkbox"/> | <input checked="" type="checkbox"/> For null hypothesis testing, the test statistic (e.g. F , t , r) with confidence intervals, effect sizes, degrees of freedom and P value noted
<i>Give P values as exact values whenever suitable.</i> |
| <input checked="" type="checkbox"/> | <input type="checkbox"/> For Bayesian analysis, information on the choice of priors and Markov chain Monte Carlo settings |
| <input checked="" type="checkbox"/> | <input type="checkbox"/> For hierarchical and complex designs, identification of the appropriate level for tests and full reporting of outcomes |
| <input checked="" type="checkbox"/> | <input type="checkbox"/> Estimates of effect sizes (e.g. Cohen's d , Pearson's r), indicating how they were calculated |

Our web collection on [statistics for biologists](#) contains articles on many of the points above.

Software and code

Policy information about [availability of computer code](#)

Data collection GSH,GSSG,cysteine, cystine and thiosulfate data was collected on HPLC, Agilent 1100 Series . [35S]-Methionine and thiosulfate radioactivity was collected on Beckman Coulter 6500 Multipurpose Scintillation Counter. Metabolomics data was collected on Agilent Masshunter Workstation Software LC/MS Data Acquisition for 6400 Series Triple Quadrupole MS with version B.08.02. Cell counts was collected on Cellometer Autocounter 3.3.9.5. Fluorescent images was collected on Zeiss LSM800 confocal microscope. Immunoblot data was collected on kwikQuant imager. Glucose and lactate data was collected on Tecan Safire 2. Immunohistochemistry data was collected on Panoramic scanner and software Slide Center 3.1. Laser doppler imaging data was collected on Perimed Laser Doppler scanning system. Flow cytometry was performed SH800 series running on software version 2.1.0.

Data analysis All software used are commercially or publicly available. GraphPad Prism 10.0 was used for the statistical tests. Microsoft Excel (Version 16.71) was used for calculations. Chem Station for LC 3D system B.03.01 software and C.01.11 OpenLab CDS was used for targeted metabolite analysis. Tube formation assay was analysed by Image J 1.53t, JAVA 1.8.0_345, 64-bit (angiogenesis plugin). Tip cell number was quantified by MATLAB image analysis code available to download from Github website (<https://github.com/hirakih/Sulfide-oxidation-promotes-hypoxic-angiogenesis-and-neovascularization-MATLAB-Code>). IHC analysis was performed on CaseViewer 1.4.

For manuscripts utilizing custom algorithms or software that are central to the research but not yet described in published literature, software must be made available to editors and reviewers. We strongly encourage code deposition in a community repository (e.g. GitHub). See the Nature Portfolio [guidelines for submitting code & software](#) for further information.

Data

Policy information about [availability of data](#)

All manuscripts must include a [data availability statement](#). This statement should provide the following information, where applicable:

- Accession codes, unique identifiers, or web links for publicly available datasets
- A description of any restrictions on data availability
- For clinical datasets or third party data, please ensure that the statement adheres to our [policy](#)

All data generated and analyzed in this study are included in the main text and Supplementary Information file. Source data are provided.

Human research participants

Policy information about [studies involving human research participants and Sex and Gender in Research](#).

Reporting on sex and gender

N/A

Population characteristics

N/A

Recruitment

N/A

Ethics oversight

N/A

Note that full information on the approval of the study protocol must also be provided in the manuscript.

Field-specific reporting

Please select the one below that is the best fit for your research. If you are not sure, read the appropriate sections before making your selection.

Life sciences Behavioural & social sciences Ecological, evolutionary & environmental sciences

For a reference copy of the document with all sections, see [nature.com/documents/nr-reporting-summary-flat.pdf](https://www.nature.com/documents/nr-reporting-summary-flat.pdf)

Life sciences study design

All studies must disclose on these points even when the disclosure is negative.

Sample size

All the experiments were performed using sample sizes based on standard protocol in the field. No statistical test were performed to predetermine the sample size. We used statistical analysis consistent with the size of samples that gave sufficient statistical power for analysis.

Data exclusions

No data was excluded.

Replication

All experimental data were reproduced in multiple independent experiments that are also mentioned in the figure legends. For in vivo experiments, multiple mice were used to ensure reproducibility. Tumor angiogenesis studies were replicated in multiple experiments.

Randomization

Sample groups were allocated randomly.

Blinding

Investigators were blinded for group allocation as the Cre negative and positive mice were mixed in the cage. Hind limb ischemia experiment was performed at core facility where genotype information was not disclosed to the technician.

Reporting for specific materials, systems and methods

We require information from authors about some types of materials, experimental systems and methods used in many studies. Here, indicate whether each material, system or method listed is relevant to your study. If you are not sure if a list item applies to your research, read the appropriate section before selecting a response.

Materials & experimental systems

n/a	Involvement
<input type="checkbox"/>	<input checked="" type="checkbox"/> Antibodies
<input type="checkbox"/>	<input checked="" type="checkbox"/> Eukaryotic cell lines
<input checked="" type="checkbox"/>	<input type="checkbox"/> Palaeontology and archaeology
<input type="checkbox"/>	<input checked="" type="checkbox"/> Animals and other organisms
<input checked="" type="checkbox"/>	<input type="checkbox"/> Clinical data
<input checked="" type="checkbox"/>	<input type="checkbox"/> Dual use research of concern

Methods

n/a	Involvement
<input checked="" type="checkbox"/>	<input type="checkbox"/> ChIP-seq
<input type="checkbox"/>	<input checked="" type="checkbox"/> Flow cytometry
<input checked="" type="checkbox"/>	<input type="checkbox"/> MRI-based neuroimaging

Antibodies

Antibodies used	Rabbit-anti-eNOS (Cell Signaling Technology, 9572S), Rabbit-anti-HIF-1 α (Abcam, ab179483), Rabbit-anti-HIF-2 α (Bethyl Lab, A700-003), Rabbit-anti-SQOR (Proteintech, 17256-1AP), Rabbit-anti-Ki67 (Cell Signaling Technology, 12202T), Rabbit-anti-CD31 (Proteintech, 28083-1AP) anti-Flag (F1804, Sigma) anti-rabbit horseradish peroxidase-linked IgG antibody (GE Healthcare, NA944V for immunoblots, and Cell signaling Technology 7074S for IHC), DyLight 649 labeled anti-Ulex europaeus Agglutinin-1 (Vector Labs, DL-1068-1), CD45-APC-eFluor 780 is from invitrogen (eBioscience), catalog number is 47-0451-82, clone name is 30-F11 and lot number is 2375407, CD31 (PECAM-1) PE is from invitrogen (eBioscience), catalog number is 12-0311-82, and lot number is 2633378.
Validation	Antibodies were validated by the manufacturer, previous studies by other groups or studies published by our lab. eNOS was validated by Cell Signaling Technology using bovine aortic endothelial cells lysate. HIF-1 α was validated by Abcam using HAP1 cell lysate in the presence and absence of HIF1 inducer DMOG. HIF-2 α was validated by Bethyl Lab in HepG2 lysates in the presence of CoCl ₂ . Ki67 was validated by Cell Signaling Technology using IHC in mice colon, heart and spleen. CD31 was validated by Proteintech in mice spleen lysate. Flag was validated by Sigma in kidney epithelial cells transfected with Flag tagged myr-PKC ζ and previous studies from our lab. UEA-1 was validated in colon carcinoma tissue sections by Vector Labs. Anti-SQOR antibody is validated by Proteintech in HeLa, HepG2 and HT29 cell lysates. As mentioned by Proteintech on their website that anti-SQOR has reactivity against human, mouse, rat, chicken and pig. CD31 (PECAM-1) was verified by Cell treatment to ensure that the antibody binds to the antigen stated. CD45-APC-eFluor 780 was validated by manufactures in C57BL/6 mouse bone marrow cells. We included SQOR and ETHE1 protein to test the specificity of anti-SQOR and anti-ETHE1.

Eukaryotic cell lines

Policy information about [cell lines and Sex and Gender in Research](#)

Cell line source(s)	The following cell lines used in our study, were purchased from ATCC-Ea.hy926 (CRL 2922), HMEC-1 (CRL-3243), HUVEC (PCS-100-013), HEK 293 (CRL-1573), Hep G2 (HB-8065), SH-SY5Y (CRL-2266). The 143B cybrid was a gift from Matthew Vander Heiden (MIT), which they have described in Sullivan L.B. et al (2015) Cell 162:552
Authentication	Cell lines were authenticated by ATCC through STR profiling.
Mycoplasma contamination	All cell lines tested negative for mycoplasma and this was done routinely with PCR based test.
Commonly misidentified lines (See ICLAC register)	No commonly misidentified cell lines were used.

Animals and other research organisms

Policy information about [studies involving animals; ARRIVE guidelines](#) recommended for reporting animal research, and [Sex and Gender in Research](#)

Laboratory animals	Both male and female C57BL/6 mice were included in the study. Mice were 8-10 weeks old. An inducible whole body disruption of <i>sqrld</i> was generated by crossing <i>Sqrld loxP/loxP</i> mice with CAGG-CreER mice (Jax # 004682). An inducible endothelial-specific disruption of <i>sqrld</i> was generated by crossing <i>SqrldloxP/loxP</i> with VE-Cadherin-CreERT2. <i>Sqrld loxP/+</i> mice were generated by Cyagen Biosciences. Mice were maintained under standard housing conditions with ad libitum access to food and water and 12h light-day cycle. Cages were cleaned every 4-5 days.
Wild animals	This study did not involve wild animals.
Reporting on sex	Both male and females included in the study.
Field-collected samples	Not applicable
Ethics oversight	All mice studies were performed with the approval from Institutional Animal Care and Use Committee (IACUC) at the University of Michigan.

Note that full information on the approval of the study protocol must also be provided in the manuscript.

Plots

Confirm that:

- The axis labels state the marker and fluorochrome used (e.g. CD4-FITC).
- The axis scales are clearly visible. Include numbers along axes only for bottom left plot of group (a 'group' is an analysis of identical markers).
- All plots are contour plots with outliers or pseudocolor plots.
- A numerical value for number of cells or percentage (with statistics) is provided.

Methodology

Sample preparation

Lungs were harvested from four mice from each of the two groups: Sqrdlfl/fl and VE-CadherinCre-ERT2 Sqrdlfl/fl. First, mice were perfused transcardially for 5 min at 2 mL/min with ice cold PBS and then with dispase solution (0.25 U/mL). Lungs were harvested and cut into small pieces with a pair of scissors and digested while shaking in dissociation solution (PBS) containing collagenase type I (5 mg/mL) and DNase I (1 mg/mL) at 37C for 45 min. The sample was then homogenized by passing through a 28G needle multiple times and then through a 70 microns filter (Fisherbrand, Sterile Cell Strainer). Red blood cell lysis was performed with ACK lysis buffer (Gibco) for 5 min and stopped with PBS + 2 % FBS (FACS buffer). Centrifugation was performed at 400 x g for 5 min and the cell pellet was incubated with anti-mouse-CD45- APC (1:100) and anti-mouse-CD31-PE (1:100) for 45 min at 4C. After staining, cells were washed twice with FACS buffer and resuspended in 3 mL of PBS.

Instrument

SH800S Cell Sorter, Sony Biotechnology

Software

SH800 software 2.1.0, created by Sony

Cell population abundance

The Leukocytes (CD45+CD31+) accounted about ~ 50% of the total cell population of the sample whereas the endothelial cells accounted for ~ 25% of the cell population. Post-sorting the purity was checked for each sorted fraction and estimated between 85-90% pure cells.

Gating strategy

The cells were gated on Forward scatter Vs Back scatter to identify the total cell population excluding debris. They were further gated on Forward scatter width Vs Area and Back scatter width Vs Area to exclude doublets. They were then gated on CD31 positivity and CD45 negative (endothelial cell population) and CD31 and CD45 positivity (Leukocyte population). Both of these gated populations were sorted via 2-way sorting method.

- Tick this box to confirm that a figure exemplifying the gating strategy is provided in the Supplementary Information.